Defining Mesoscale Eddies Boundaries from In-situ Data and a Theoretical Framework

Yan Barabinot[1], Sabrina Speich[1], and Xavier J. Carton[2]

[1]Ecole Normale Supérieure
[2]Universite de Bretagne Occidentale

March 13, 2023

Abstract

Mesoscale eddies are found throughout the global ocean. Generally, they are referred to as "coherent" structures because they are organized rotating fluid elements that propagate within the ocean and have a long lifetime. Since in situ observations of the ocean are very rare, eddies have been characterized primarily from satellite observations or by relatively idealized approaches of geophysical fluid dynamics. Satellite observations provide access to only a limited number of surface features and exclusively for structures with a fingerprint on surface properties. Observations of the vertical sections of ocean eddies are rare. Therefore, important eddy properties, such as eddy transports or the characterization of eddy "coherence", have typically been approximated by simple assumptions or by applying various criteria based on their velocity field or thermohaline properties. In this study, which is based on high-resolution in-situ data collection from the EUREC4A-OA field experiment, we show that Ertel potential vorticity is very appropriate to accurately identify the eddy core and its boundaries. This study provides evidence that the eddy boundaries are relatively intense and intimately related to both the presence of a different water mass in the eddy core from the background and to the isopycnal steepening caused by the volume of the eddy. We also provide a theoretical framework to examine their orders of magnitude and define an upper bound for the proposed definition of the eddy boundary. The results suggest that the eddy boundary is not a well-defined material boundary but rather a frontal region subject to instabilities.

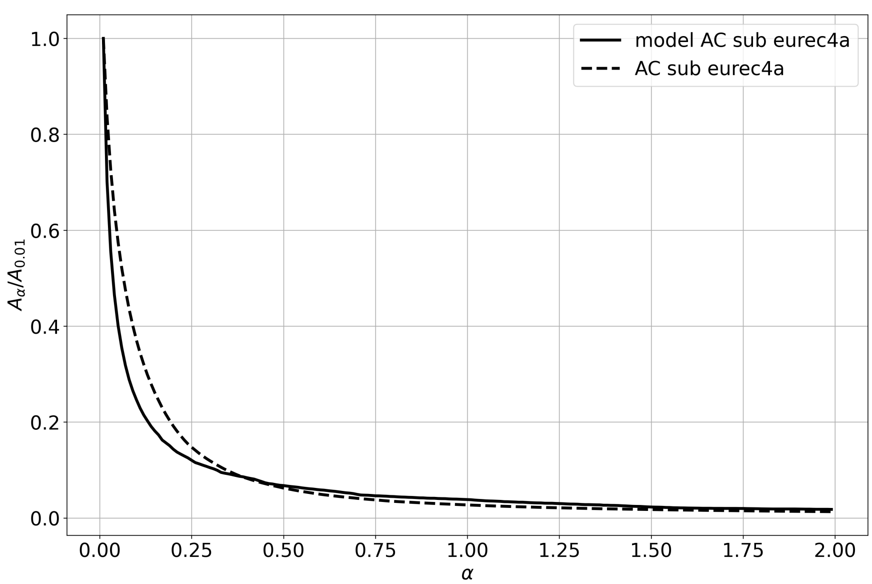

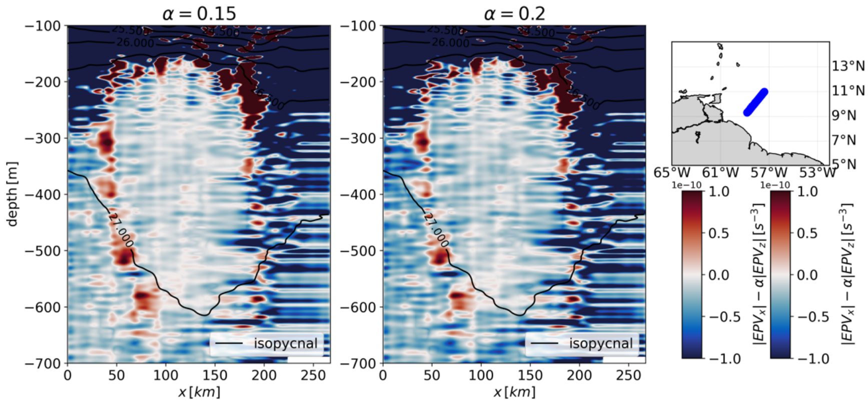

$\alpha = 0.15$
$\alpha = 0.2$
depth [m]
$x\,[km]$
isopycnal
25.500
26.000
27.000
13°N
11°N
9°N
7°N
5°N
65°W
61°W
57°W
53°W
1e−10
$|EPV_x| - \alpha|EPV_z|\,[s^{-3}]$

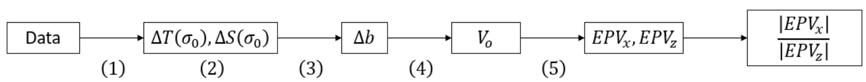

Data
$\Delta T(\sigma_0), \Delta S(\sigma_0)$
Δb
V_o
EPV_x, EPV_z
$\frac{|EPV_x|}{|EPV_z|}$
(1)
(2)
(3)
(4)
(5)

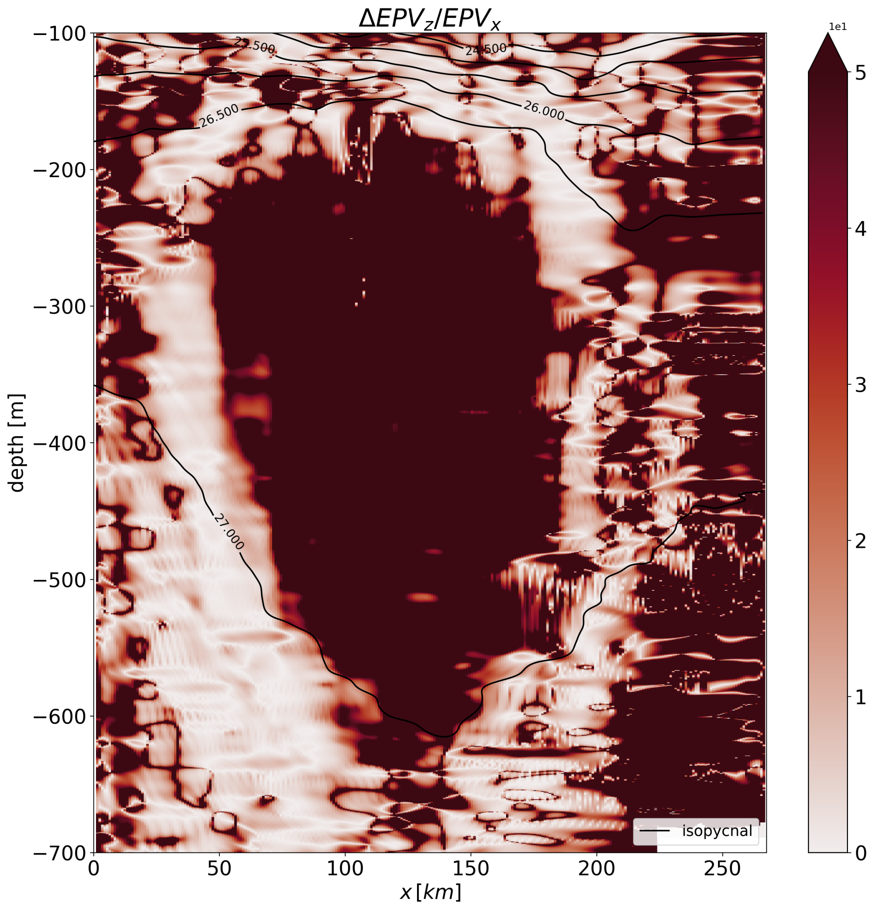

$\Delta EPV_z/EPV_x$
depth [m]
$x\,[km]$
isopycnal
25.500
26.000
26.500
27.000
1e1

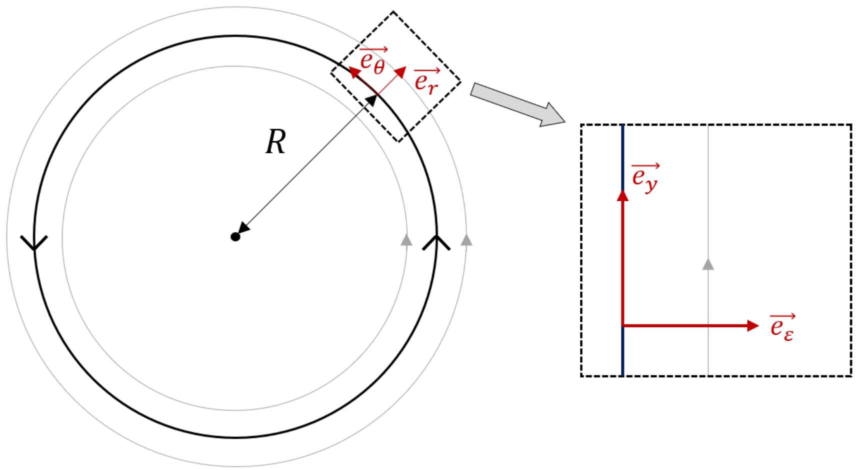
R
$\vec{e_\theta}$
$\vec{e_r}$
$\vec{e_y}$
$\vec{e_\varepsilon}$

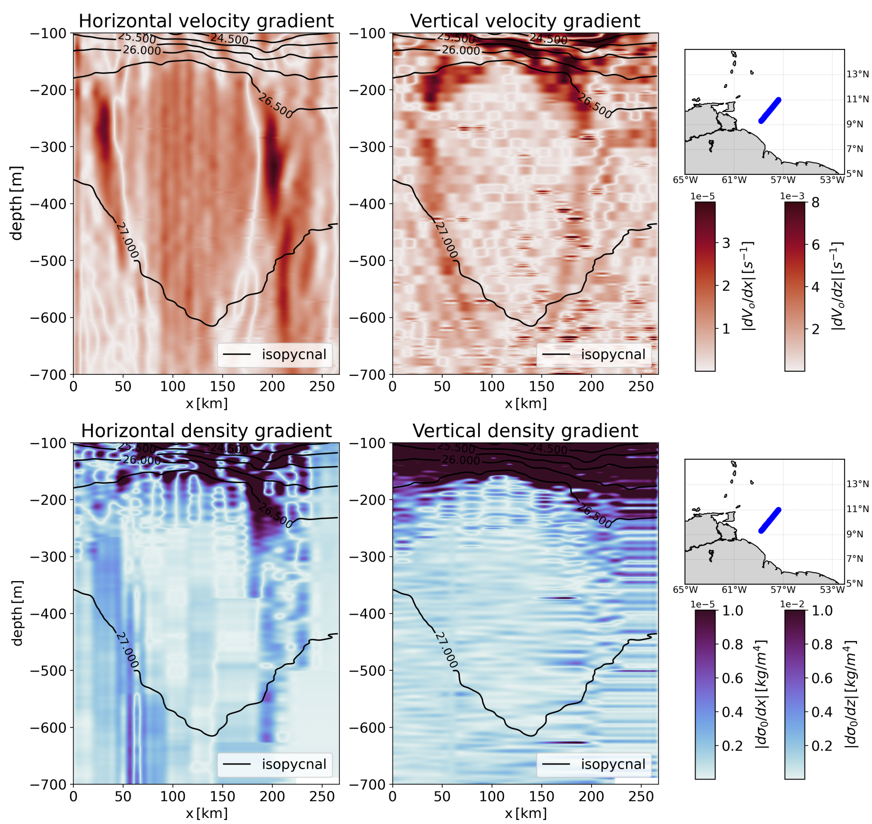
Horizontal velocity gradient
Vertical velocity gradient
Horizontal density gradient
Vertical density gradient
depth [m]
x [km]
isopycnal
24.500
25.500
26.000
26.500
27.000
$|dV_o/dx|\,[s^{-1}]$
$|dV_o/dz|\,[s^{-1}]$
$|d\sigma_0/dx|\,[kg/m^4]$
$|d\sigma_0/dz|\,[kg/m^4]$

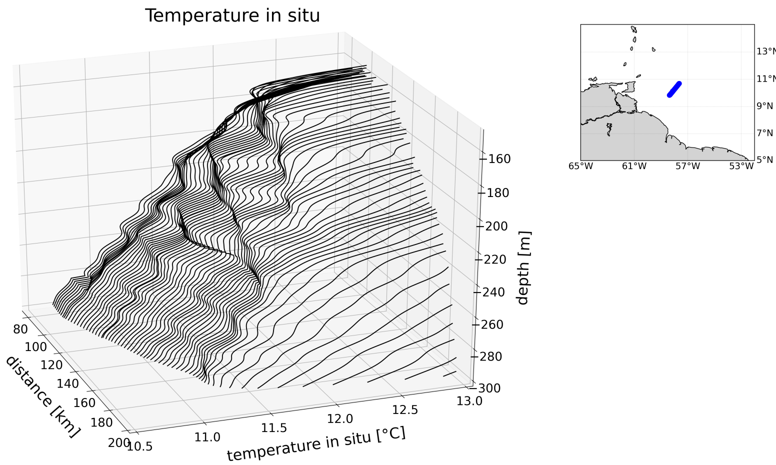
Temperature in situ
distance [km]
temperature in situ [°C]
depth [m]
13°N
11°N
9°N
7°N
5°N
65°W
61°W
57°W
53°W

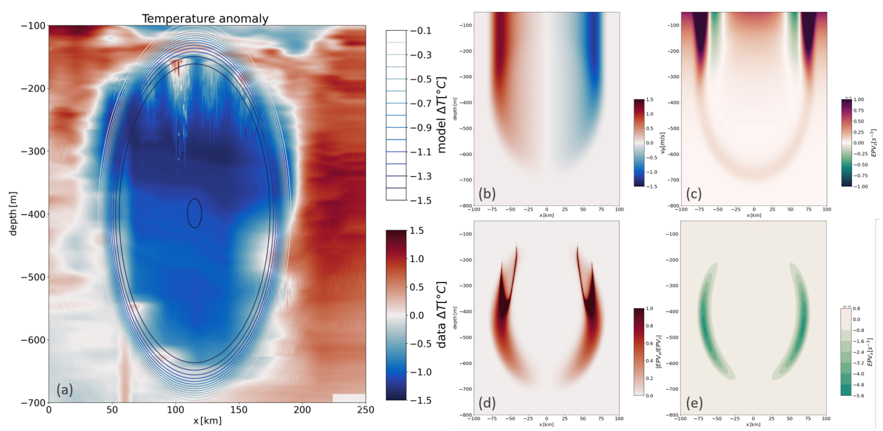
Temperature anomaly
depth [m]
x [km]
model ΔT[°C]
data ΔT[°C]
(a)
(b)
(c)
(d)
(e)

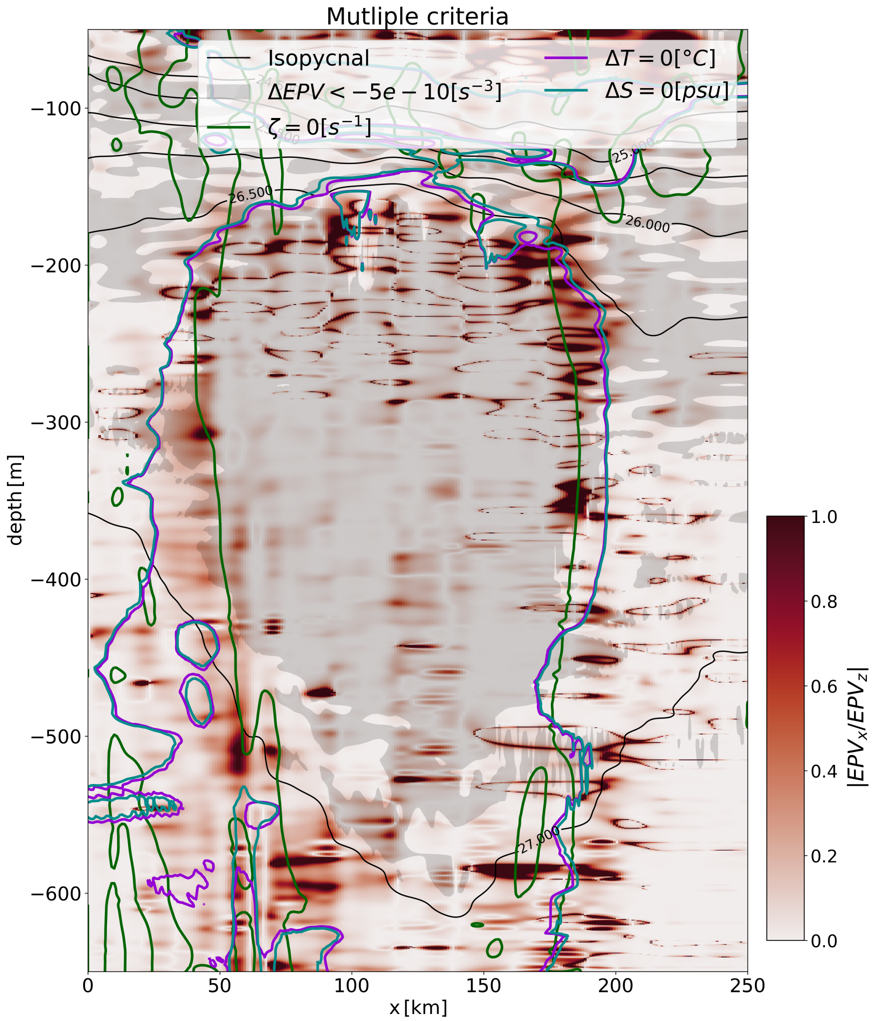

Mutliple criteria
Isopycnal
$\Delta EPV < -5e-10[s^{-3}]$
$\zeta = 0[s^{-1}]$
$\Delta T = 0[°C]$
$\Delta S = 0[psu]$
26.500
26.000
27.000
depth [m]
x [km]
$|EPV_x/EPV_z|$

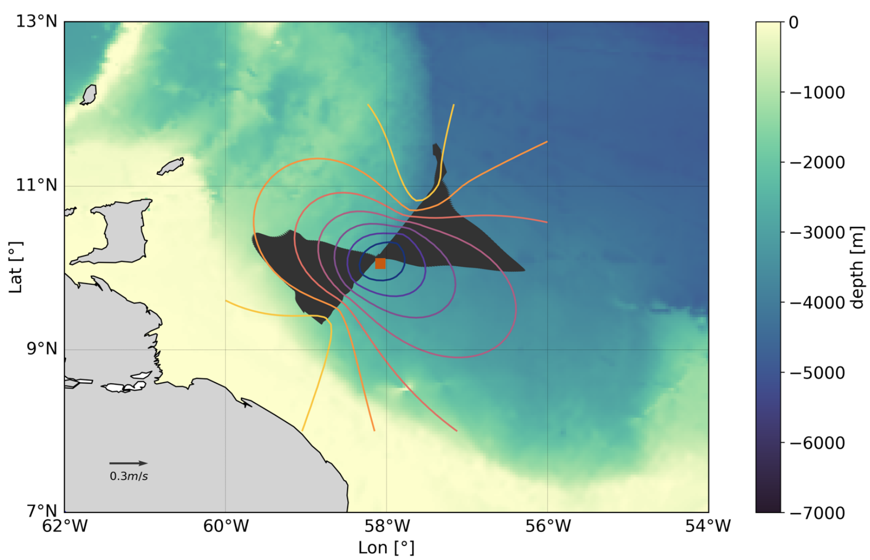

13°N
11°N
9°N
7°N
62°W
60°W
58°W
56°W
54°W
Lat [°]
Lon [°]
0.3m/s
depth [m]

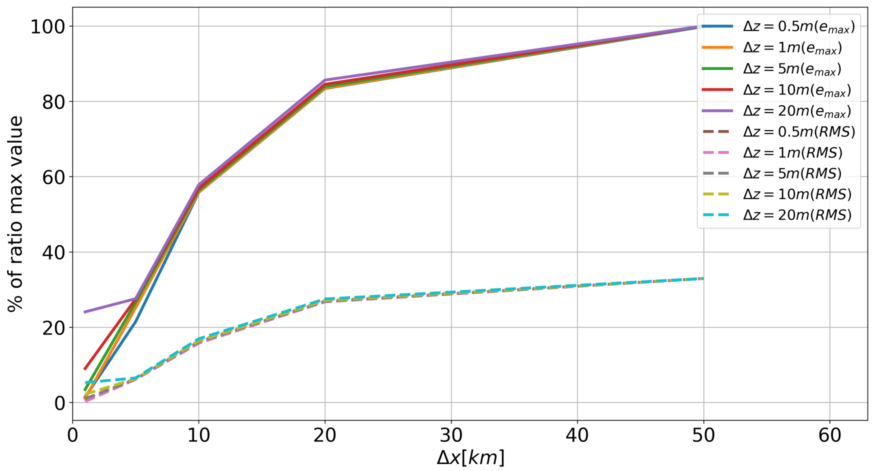
% of ratio max value
$\Delta x[km]$
$\Delta z = 0.5m(e_{max})$
$\Delta z = 1m(e_{max})$
$\Delta z = 5m(e_{max})$
$\Delta z = 10m(e_{max})$
$\Delta z = 20m(e_{max})$
$\Delta z = 0.5m(RMS)$
$\Delta z = 1m(RMS)$
$\Delta z = 5m(RMS)$
$\Delta z = 10m(RMS)$
$\Delta z = 20m(RMS)$

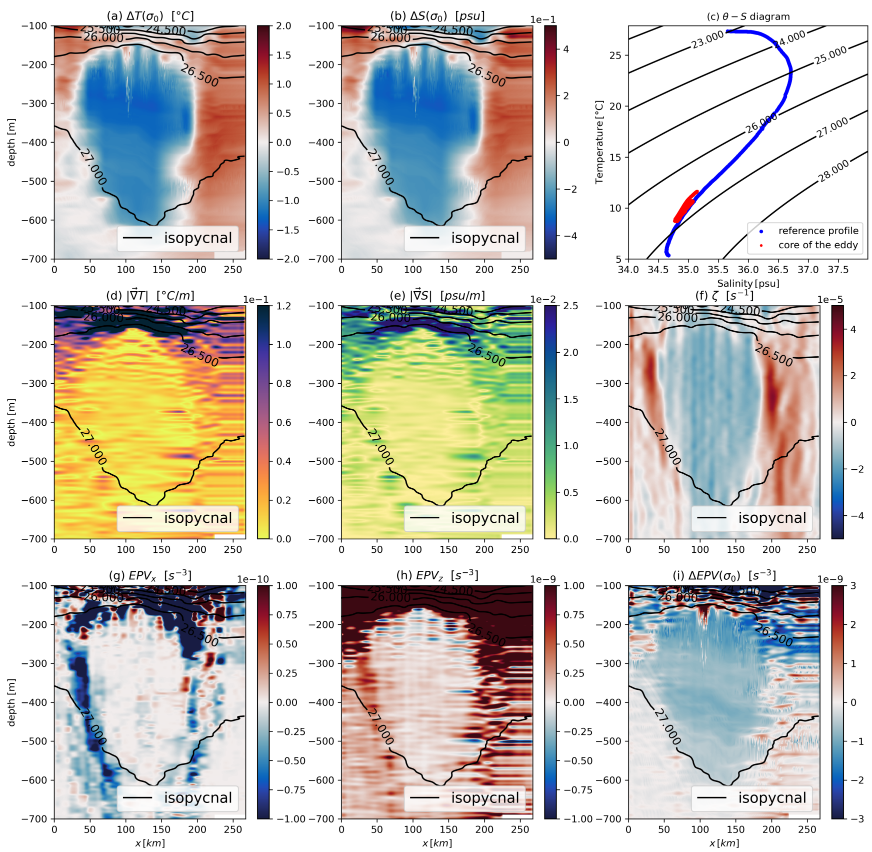
(a) $\Delta T(\sigma_0)$ [°C]
(b) $\Delta S(\sigma_0)$ [psu]
(c) $\theta - S$ diagram
(d) $|\vec{\nabla} T|$ [°C/m]
(e) $|\vec{\nabla} S|$ [psu/m]
(f) ζ [s^{-1}]
(g) EPV_x [s^{-3}]
(h) EPV_z [s^{-3}]
(i) $\Delta EPV(\sigma_0)$ [s^{-3}]
depth [m]
x [km]
Temperature [°C]
Salinity [psu]
isopycnal
reference profile
core of the eddy

Defining Mesoscale Eddies Boundaries from In-situ Data and a Theoretical Framework

Yan Barabinot[1], Sabrina Speich[1], Xavier Carton[2]

[1]Ecole Normale Supérieure, Laboratoire de Météorologie Dynamique (LMD), 24 rue Lhomond, Paris 75005, France
[2]Université de Bretagne Occidentale (UBO), Laboratoire d'Océanographie Physique et Spatial (LOPS), IUEM, rue Dumont Durville, Plouzané 29280, France

Key Points:

- Various definitions of eddy boundaries are explored using the EUREC^{4}A-OA experiment high-resolution collection of in-situ data
- Eddy boundaries behave like a front
- A theoretical framework is provided to examine orders of magnitude of physical variables at the boundary

Corresponding author: Yan Barabinot, `yan.barabinot@ens-paris-saclay.fr`

Abstract

Mesoscale eddies are found throughout the global ocean. Generally, they are referred to as "coherent" structures because they are organized rotating fluid elements that propagate within the ocean and have a long lifetime. Since in situ observations of the ocean are very rare, eddies have been characterized primarily from satellite observations or by relatively idealized approaches of geophysical fluid dynamics. Satellite observations provide access to only a limited number of surface features and exclusively for structures with a fingerprint on surface properties. Observations of the vertical sections of ocean eddies are rare. Therefore, important eddy properties, such as eddy transports or the characterization of eddy "coherence", have typically been approximated by simple assumptions or by applying various criteria based on their velocity field or thermohaline properties. In this study, which is based on high-resolution in-situ data collection from the EUREC4A-OA field experiment, we show that Ertel potential vorticity is very appropriate to accurately identify the eddy core and its boundaries. This study provides evidence that the eddy boundaries are relatively intense and intimately related to both the presence of a different water mass in the eddy core from the background and to the isopycnal steepening caused by the volume of the eddy. We also provide a theoretical framework to examine their orders of magnitude and define an upper bound for the proposed definition of the eddy boundary. The results suggest that the eddy boundary is not a well-defined material boundary but rather a frontal region subject to instabilities.

Plain Language Summary

Mesoscale eddies are ubiquitous rotating flows in the ocean. They are considered as one of the major sources of ocean variability as they can live for months, transporting and mixing heat, salt and other properties within and among ocean basins. They have been extensively studied through satellite observations as they are often located at or close to the ocean surface. However, observations of their 3D structure are rare and computation of eddy transport are often approximated without a precise knowledge of their real vertical extension. Moreover, recent studies suggest the existence of subsurface eddies that are indiscernible in satellite observations. Here, by analyzing high-resolution observations collected during the large EUREC4A-OA field experiment in the northwestern tropical Atlantic Ocean, we propose a new criterion that is based on geophysical fluid dynamics theory and appears to define the lateral and vertical eddies boundaries particularly well. This criterion can be applied widely to gather careful assessment of eddy structure, volume, transport and their evolution. We also provide insight into why these boundaries are substantial, which may explain why oceanic eddies are coherent structures that can have long lifetimes. Furthermore, we show that eddy boundaries are not quiescent zones but turbulent limited-area region.

1 Introduction

In the ocean, mesoscale eddies have been observed and sampled for several decades, via in-situ and satellite measurements. They are defined as relatively long-lasting horizontal recirculations of seawater, over a spatial scale close to one or a few deformation radii, and smaller than the Rhines scale (Rhines, 1975). Since the 1990's, satellite observations (in particular altimetry) have been used to detect ocean mesoscale eddies, to evaluate their intensity, their life time and their trajectories (Chaigneau et al., 2009; Chelton et al., 2011). The number, lifetime and structure of mesoscale eddies have also been assessed via the trapping of surface drifters (Lumpkin, 2016), of acoustically tracked floats (Richardson & Tychensky, 1998), or of vertically profiling Argo floats (Nencioli et al., 2016; Laxenaire et al., 2019, 2020). This lifetime often exceeds several months and may reach several years (Laxenaire et al., 2018; Ioannou et al., 2022). Such a long lifespan suggests that most ocean mesoscale eddies are resilient dynamical structures.

One of the most important properties of mesoscale eddies is their ability to trap water masses at their generation sites and to transport them over very long periods of time and distances. Indeed, due to their quasi-2D recirculating fluid motions, water mass in the eddy core remain constrained by closed trajectories created by the azimuthal velocity field. This phenomenon was first described by Flierl (1981) when floats became an important tool for measuring ocean processes. Using a Lagrangian approach, he suggested that when the azimuthal average velocity field is larger than the translation speed of the eddy, then fluid particles are trapped in the core of the eddy. As a result, the water mass in the vortex core often differs from surrounding water masses and are thus associated with temperature/salinity anomalies (e.g., L'Hégaret, Carton, et al., 2015; L'Hégaret, Duarte, et al., 2015; Laxenaire et al., 2019, 2020; Ioannou et al., 2022).

Therefore, mesoscale eddies are thought to play a major role in the transport of properties (heat, salt, carbon, and other chemical components) as they propagate through the ocean, representing a key dynamic element in the overall global budget of these tracers (Bryden, 1979; Jayne & Marotzke, 2002; Morrow & Traon, 2012; Wunsch, 1999). Moreover, mesoscale eddies impact all the different dynamical components of the ocean, from air-sea fluxes (Frenger et al., 2013) to the ventilation of the ocean interior (Sallée et al., 2010) and the large-scale ocean circulation (Morrow et al., 1994; Lozier, 1997). Due to temperature/salinity differences between the water masses trapped within eddies and those outside them, the eddy boundaries have been often characterized as large gradients of thermohaline properties resulting in finite-gradient regions (Pinot et al., 1995; Martin et al., 2002; Chen et al., 2020). There, the variance increases and one can think that the diffusion of the tracer also intensifies. However, even in the case of turbulent diffusion, this process is very slow in the ocean (turbulent diffusion coefficients are of the order of $10^{-4} m/s^2$ in the case of mesoscale eddies). Ruddick and Gargett (2003) and Ruddick et al. (2010) showed that lateral mixing was mostly generated by lateral intrusions for axisymmetric meddies. The horizontal diffusion coefficient on the boundary of the eddy was estimated at $10^{-5} m/s^2$ which is very low compared to diffusive processes in other media. Therefore, for an isolated eddy, the initially trapped water mass inside the core can remain unaltered for long periods.

Using mainly satellite altimetry fields, previous studies have attempted to quantify eddy transport by using proxies to calculate eddy volumes. Eulerian and Lagrangian criteria were used to obtain an overall estimate of the impact of eddies on tracer transport (Hunt et al., 1988; Ōkubo, 1970; Weiss, 1991; Beron-Vera et al., 2013). Although the development of satellite altimetry has brought a real advance in the monitoring of eddies in the ocean, it only gives access to smoothed (in time and space) sea-surface height. Surface geostrophic velocities are derived from the latter. They do not often correspond to the effective eddy core velocities. This is partly due to the space-time resolution and smoothing applied to satellite altimetry products, but also to the fact that eddies detected from satellite altimetry are not always surface intensified eddies (their core can lie well below the ocean surface and mixed layer). This suggests that satellite data, iclud-ing satellite altimetry, might not suffice to represent the kinematics and dynamical properties of eddies nor their 3D properties. Therefore, the large set of Eulerian and Lagrangian eddy estimates available from satellite data alone do not always adequately describe the characteristics and evolution of ocean eddies.

To better understand the properties and behavior of eddies, we rely on very high resolution in-situ observations collected during the EUREC4A-OA experiment in January-February 2020 in the tropical northwest Atlantic, as well as on a theoretical framework. We propose to define the 3D boundary of mesoscale eddies using a new criterion based on the Ertel Potential Vorticity (EPV) (Ertel, 1942). The EPV is indeed a powerful tool to study ocean dynamics. It combines in its definition both, the existence of closed trajectories inside eddies in which it remains invariant (in the absence of forcing and mixing) and its their impermeability in terms of trapping of water masses (via the isopycnical deflections). In the ocean, EPV mixing occurs at its boundaries (surface, bottom, and straits/passages where inflows/outflows of water take place) (Welander, 1973; Benthuysen & Thomas, 2012). EPV mixing develops also at eddy boundaries and fronts. Moreover, previous studies of potential vorticity dynamics have quantified the impact of forcing and mixing processes on the EPV distribution (Marshall & Schott, 1999; Marshall & Speer, 2012). In this study, we show how EPV can be used to define the 3D eddy boundary.

The paper is organized as follows. In Section 2, we describe the in-situ data we use. In Section 3, we explore how eddy boundaries have been previously defined and we describe a particularly well-sampled by in-situ data subsurface eddy. In Section 4, we introduce the criterion we developed to define the eddy boundaries based on observations. In Section 5, using a generic eddy, we evaluate the order of magnitude of the criterion we have defined to support the observations. In the appendix, we also propose a constrain to this criterion using a theoretical framework for semi-geostrophic baroclinic instability. In section 6, we conclude the paper by summarizing our results.

2 Data and Methods

2.1 In-situ data collected during the EUREC^{4}A-OA experiment

The EUREC^{4}A-OA campaign took place between the 20^{th} of January and the 20^{th} of February 2020 (Speich & Team, 2021). We focus here on a subsurface anticyclonic eddy, located between about 200 and 600 m depth, which was sampled along the continental slope of Guyana by the French RV L'Atalante. Hydrographic observations were carried out using Conductivity Temperature Pressure (CTD), underway CTD (uCTD) and Lower Acoustic Doppler Profiler (L-ADCP) measurements. A total of 17 vertical profiles provides access to the thermohaline and velocity properties of the eddy. The velocity field was also measured by two Ship-mounted ADCPs (S-ADCPs) with a sampling frequency of 75kHz and 38kHz. Temperature and salinity were measured by the CTD with an accuracy of respectively $\pm 0.002°C$ and $\pm 0.005psu$. For the uCTD, temperature and salinity accuracy are, respectively, $\pm 0.01°C$ and $\pm 0.02psu$. The S-ADCP measures horizontal velocities with an accuracy of $\pm 3cm/s$. See L'Hégaret et al. (2022) for more information on the in-situ data collected during the EUREC^{4}A-OA field work.

The in-situ data were collected along the vertical section encompassing the vertical profiles undertaken at various distance one from the other. We define the resolution of the vertical section as the average of all distances between successive profiles in this section. For the particular section of the subsurface anticyclonic eddy discussed in this study, hydrographic data have a horizontal (resp. vertical) resolution of $8.4km$ (resp $1m$) and velocity data have a horizontal (resp. vertical) resolution of $0.3km$ (resp. $8m$ - we use the 38 kHz S-ADCP data). In the following, depending on properties, either the resolution of hydrographic data or velocity data will be used.

For the purpose of our study, it is important that the vertical sampling section of the eddy passes through its center. In figure 1, we show, using the S-ADCP data and the eddy center detection method of Nencioli et al. (2008) that this was the case for the data we use in this study to describe the subsurface anticyclonic eddy. As mentioned above, it was important to select a subsurface eddy for which we can have access to its full boundaries (upper, lower, and lateral). In the literature, these conditions are rarely, if ever, met.

2.2 Data processing

Raw data were validated, calibrated and then interpolated (L'Hégaret et al., 2022). Interpolation of vertical profiles sampled at different times had to be achieved with caution not to create artificial field. To limit spurious effects, we only performed linear in-

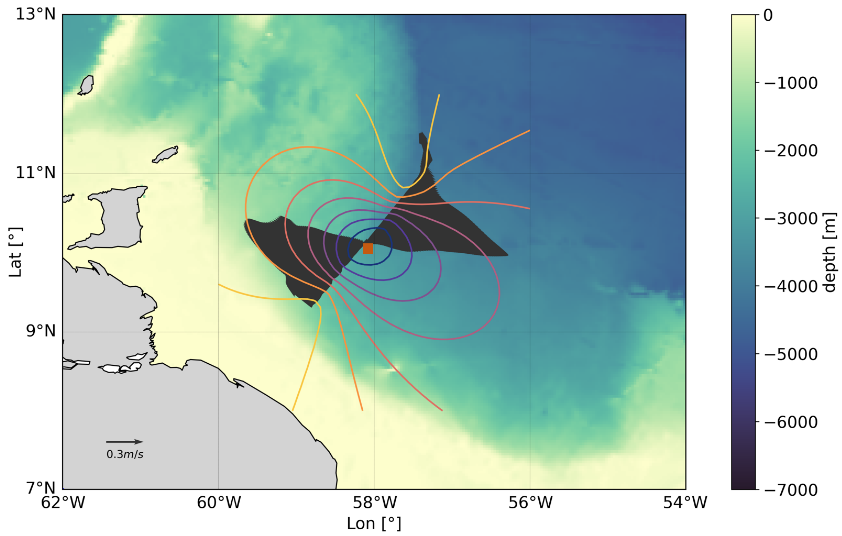

Figure 1. Velocity vector field at $-300m$ for one of the subsurface anticyclonic eddy sampled by the RV L'Atalante 38 kHz S-ADCP during the EUREC^{4}A-OA oceanographic cruise. The regional bathymetry from the ETOPO2 dataset (Smith & Sandwell, 1997) is presented in the background as color shading as well as the estimated center (the orange square) of the eddy computed from the observed velocities using Nencioli et al. (2008) method. The colored contours represent the loci of constant tangential velocity. The center is defined as the point where the average radial velocity is minimum.

terpolations in the $\vec{x}$ (here radial) and in $\vec{z}$ (vertical) directions. Then, data were smoothed using a numerical low pass filter of order 4 (scipy.signal.filt in Python). The choice of thresholds is subjective and depends on the scales studied. Here, we consider mesoscale eddies, so we choose $L_x \geq 10km$ and $L_z \geq 10m$ for the horizontal and vertical length scales. The cutoff period is chosen to be longer than the temporal sampling of the calibrated data. Therefore, the grid size chosen for the interpolated data was $(\Delta x, \Delta z) = (1km, 0.5m)$ and the data were smoothed with $L_x = 10km$ and $L_z = 10m$.

Denoting $(\vec{x}, \vec{z})$ the vertical plane of the section, and using smoothed data, the derivatives of a quantity a are approximated by a Taylor expansion of order one as follows:

$$\partial_x a(x + \Delta x, z) \approx \frac{a(x+\Delta x,z)-a(x,z)}{\Delta x},$$

$$\partial_z a(x, z + \Delta z) \approx \frac{a(x,z+\Delta z)-a(x,z)}{\Delta z}.$$

Since the Taylor expansion has been truncated, the terms

$$(a(x + \Delta x, z) - 2a(x, z) + a(x - \Delta x, z))/\Delta x^2$$

and

$$(a(x, z + \Delta z) - 2a(x, z) + a(x, z - \Delta z))/\Delta z^2$$

of order 2 are neglected. An approximation of this term for temperature, salinity, and velocity field was calculated to substantiate this point. The second order terms for temperature are, on average, about $2.10^{-9°}C/m^2$ horizontally and $1.3.10^{-4°}C/m^2$ vertically. These values are very small compared to the first order terms ($7.6.10^{-6°}C/m$ horizontally and $2.5.10^{-2°}C/m$ vertically). For salinity and orthogonal velocity, the first-order horizontal (vertical) terms are respectively higher by a factor of 10^5 (10^2) and 10^3

(10^2) than the second-order terms. With these approximations, the gradients of the different fields can be reliably calculated.

3 Eddy boundaries characterization from previous published criteria

We describe, in the following, several criteria used to determine eddy boundaries from in-situ observations in previous studies.

3.1 Relative Vorticity

The first criterion we present is based on the relative vorticity ζ. The boundary of an eddy is defined as a closed contour where ζ changes sign, or more simply where $\zeta = 0$. This criterion has often been applied to altimetry maps using geostrophic velocity (Morvan et al., 2019; D'Addezio et al., 2019). It is a simple way to provide the upper boundary of a surface eddy or the lateral boundary of a subsurface eddy. It requires a knowledge of the horizontal velocity field but it does not require any reference profile.

To derive the relative vorticity (the vertical component of the vorticity vector), derivatives in two perpendicular horizontal directions are required. With a single ship section, this is not possible. An approximation to the relative vorticity is the "Poor Man's Vorticity" (PMV) introduced by Halle and Pinkel (2003). They decomposed the measured velocities into a transverse component $v_\perp$ (denoted V_o in figure 3) and a longitudinal component $v_\parallel$. The relative vorticity is then approximated as $\zeta \approx 2\frac{\partial v_\perp}{\partial x}$. The factor of 2 allows the PMV to be equal to the actual ζ in a rotating solid body vortex core. Rudnick (2001) and Shcherbina et al. (2013) used the derivative along the section of perpendicular velocities without the factor 2. Here we retain the latter approximation:

$$\zeta \approx \frac{\partial v_\perp}{\partial x} \tag{1}$$

The errors on the relative vorticity can be calculated using finite differences. Using equation (1), a local assessment of accuracy can be obtained:

$$\frac{\Delta\zeta}{\zeta} \approx \frac{\Delta V_o}{V_o} + \frac{\Delta x}{l} \tag{2}$$

where Δx is the spacing between two measurement points (two stations) and l is a characteristic length scale taken here as the distance from the current point to the center of the eddy. Obviously, the smaller l and V are, the larger the uncertainty, which can reach unlimited values. To avoid this pitfall and obtain an order of magnitude, we fix $r = R = 71km$, $V(r) = V_0 = 0.96m/s$ (the maximum rotation speed of the eddy); the relative error on the relative vorticity is then given by:

$$\frac{\Delta\zeta}{\zeta} = \frac{\Delta V_o}{V_o} + \frac{\Delta x}{R} \tag{3}$$

By taking into account the actual resolution of the S-ADCP data, this accuracy is 3.5%. For comparison, the vertical gradient of the orthogonal velocity is estimated as $\partial_z V_o \approx \frac{V_o}{H}$, where $H = 220m$ is the maximum isopycnal displacement in the eddy core; its relative error is 6.8% for the same eddy. Here, the vertical resolution of the velocity data constrains the accuracy of our estimates.

Nevertheless, this criterion suffers from limitations. If the eddy is embedded in a parallel flow of uniform velocity U_0, a fluid particle may escape from the eddy core even if it lies inside the $\zeta = 0$ contour (the relevant kinematic criterion then includes the ratio $V(r)/U_0$). Moreover, as shown in figure 2 (panel (f)), at the upper and lower boundaries of a subsurface eddy, the velocity field can tend to zero. Criteria based on surface vorticity are then ineffective in determining the eddy boundary.

More generally, it seems counterintuitive to have a locally defined edge since an eddy boundary is a relatively broad region characterized by turbulence subject to external shear and instabilities (de Marez et al., 2020). From a Lagrangian point of view, a fluid particle located on the $\zeta/f_0 = 0$ line is in an unstable region and can be pulled into or out of the core. Finally, this criterion does not take into account the thermohaline properties of the water trapped in the core, whereas they have an impact on the global dynamics of the eddy.

3.2 Thermohaline anomalies on isopycnals

When an eddy traps and transports water masses, the temperature and salinity anomalies of the eddy core relative to the surrounding waters can help determine the eddy boundary. The eddy boundary is the region where the surrounding and trapped waters converge. Thus, a priori, temperature and salinity anomalies on isopycnic surfaces disappear there. Noting T^* and S^* as two reference temperature and salinity profiles (outside eddies) and T and S as profiles (in eddies), the thermohaline anomalies on isopycnic surfaces are defined by:

$$\forall\sigma_0, \quad \Delta T(\sigma_0) \quad = T(\sigma_0) - T^*(\sigma_0) \tag{4}$$
$$\forall\sigma_0, \quad \Delta S(\sigma_0) \quad = S(\sigma_0) - S^*(\sigma_0) \tag{5}$$

where σ_0 is the potential density referenced to the surface pressure. It is interesting to note that the compressibility of seawater is low for the studied subsurface eddy. Therefore, the T/S fields will be correlated and the anomalies will show similar structures.

The best choice of the reference profile has been the subject of several studies. Here, we use the methodology developed by Laxenaire et al. (2019). A climatological average of temperature/salinity/potential density is calculated over the geopotential levels, in a domain containing the sampled eddy. A square of side 0.5° is constructed around the estimated center of the eddy so that the center lies at the intersection of the diagonals. Then, all temperature, salinity, potential density profiles sampled by Argo profiling floats over 20 years in this area are assembled, and their values are averaged over the geopotential levels.

In figure 2, these anomalies are plotted (panels (a) and (b)) at the geopotential level. In fact, these anomalies are calculated on isopycnal surfaces but interpolated on geopotential levels to facilitate comparison with other criteria. The isopycnal deviations (dark lines) are consistent with the anticyclonic nature of the eddy. Large negative temperature and salinity anomalies occur between $150m$ and $600m$ depth, showing that a heterogeneous water mass is trapped in the eddy core. The surrounding waters are warmer and saltier than the core. Panel (c) showing the θ_S diagram confirms this statement. The anomalies appear fairly uniform in the core of the eddy and decrease near the eddy boundary. Closer inspection shows that they are slightly more intense in the upper part of the core (between 250 and 350 m depth) and slowly decrease with depth. Small-scale patterns of these anomalies are observed in the upper part of the core; they will be discussed further in part 4.2.

By means of these quantities, the boundaries of the eddy can be drawn using a zero line ΔT or ΔS (figure 1). These lines are used to locally define the upper, lower and lateral boundaries of the eddy. If thermohaline exchange is considered to occur at the boundary of an eddy, this boundary is actually spread out rather than point-like. Furthermore, the null lines are also sensitive to the reference profiles and will therefore vary by choosing different T^* and S^*.

At the eddy boundary, the gradients of T and S defined as :

$$|\vec{\nabla}(T,S)| = \sqrt{(\partial_x(T,S))^2 + (\partial_z(T,S))^2} \tag{6}$$

increase (see Fig 2 (d), (e)). Characterizing the eddy boundary in terms of temperature or salinity gradient has two advantages over T or S anomalies: first, the region of intense T or S gradients is not point-like but widespread; second, they do not depend on a reference value.

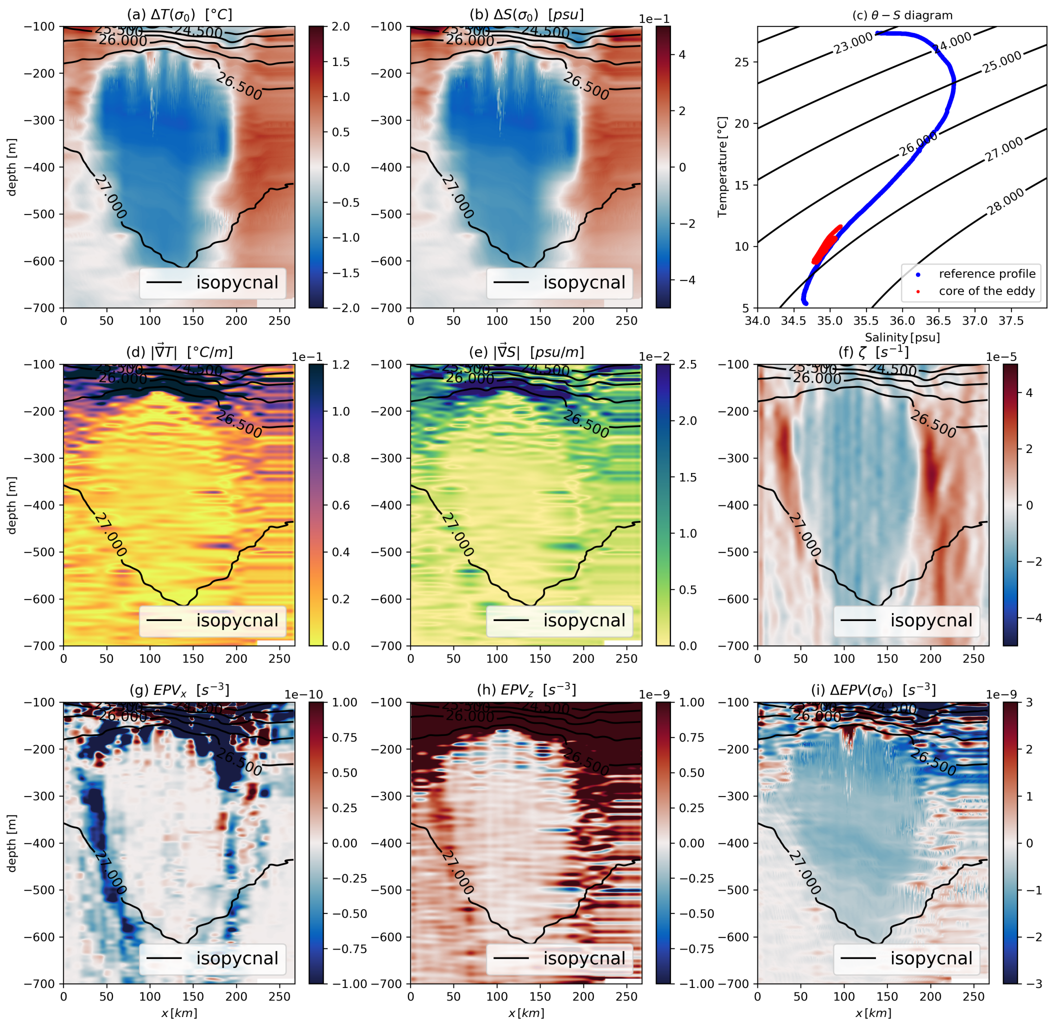

Figure 2. Vertical sections (x-axis = horizontal scale, z-axis = vertical scale) of various quantities : (a) thermal anomaly on isopycnal surfaces interpolated on geopotential level; (b) salinity anomaly on isopycnal surfaces interpolated on geopotential level; (c) $\theta - S$ diagram; (d) and (e) norm of 2D temperature/salinity gradients; (f) relative vorticity; (g) horizontal component of EPV; (h) vertical component of EPV; (i) EPV anomaly on isopycnal surfaces interpolated on geopotential level. The thermohaline anomalies computed on isopycnals are showing a maximum at depth. For the $\theta - S$ diagram the reference profile in blue is the climatological average computed using ARGO floats and the red dots represent grid points for $x \in [100km; 150km]$ and $z \in [-400m; -300m]$. Data have been smoothed with a cutoff of $10km$ horizontally and $10m$ vertically. Isopycnals are plotted in dark lines. The core is characterized by an homogeneous negative relative vorticity and EPV anomaly as well as negative thermohaline anomalies.

3.3 Ertel Potential Vorticity on isopycnals (EPV)

Ocean eddies are associated with a rotating flow field around an axis, with closed current lines and with thermohaline anomalies due to the water mass trapped in their cores. Ertel's Potential Vorticity (EPV) (Ertel, 1942) which takes into account all these properties has therefore often been used to characterize the structure of eddies. The EPV is a Lagrangian invariant under several assumptions: inviscid flow, incompressible fluid and potential body forces (Egger & Chaudhry, 2009). In the ocean, the EPV is rarely conserved because of atmospheric forcing and energy dissipation (Morel et al., 2019). For subsurface eddies, far from the ocean floor, changes in EPV are moderate during most of their life cycle.

EPV is defined in general for 3D, non hydrostatic flows with arbitrary density fluctuations. Here, we simplify this general definition for an application to 2D in-situ data. We also apply the Boussinesq approximation and the hydrostatic balance. Under these hypotheses, the vertical acceleration vanishes and in the EPV definition, the term $1/\sigma_0 \approx 1/\sigma_0^{(0)}$, with $\sigma_0^{(0)} = 1026.4 kg/m^3$ a reference value taken here as the average over every profile of the section. With our simplifications, EPV takes the following form:

$$EPV = EPV_x + EPV_z = (-\partial_z V_o \partial_x b) + (\partial_x V_o + f)\, \partial_z b \tag{7}$$

where $b = -g\frac{\sigma_0}{\sigma_0^{(0)}}$ is the buoyancy and V_o denotes the orthogonal component of the velocity at the horizontal axis of the section. Note that, although equation (7) only provides a 2D approximation of the real value of EPV, no approximation on the shape of the eddy has been used (axisymmetry for example). We can also compute the relative error on the quantity introduced. The uncertainty is given by :

$$\frac{\Delta EPV_x}{EPV_x} = \frac{\Delta_H b}{b} + \frac{\Delta_H x}{l} + \frac{\Delta_V V_o}{V_o} + \frac{\Delta_V z}{\Delta z} \tag{8}$$

$$\frac{\Delta EPV_z}{EPV_z} = \frac{\Delta_H b}{b} + \frac{\Delta_H z}{H} + \frac{\Delta_V V_o}{V_o} + \frac{\Delta_V x}{l} \tag{9}$$

where, Δ_H refers to the uncertainty in the hydrological data and Δ_V to the uncertainty in the velocity data. To calculate the uncertainty in buoyancy, we use the linearized equation of state:

$$\Delta_H b = \frac{-g}{\sigma_0^{(0)}} \Delta_H \sigma_0 = \frac{-g}{\sigma_0^{(0)}} (-\alpha \Delta_H T + \beta \Delta_H S) \tag{10}$$

where g is gravity, α and β are average values over the ship's section. This approach leads to an error of 18.6% for EPV_x and 3.8% for EPV_z. Obviously, this is an order of magnitude and, as before, the horizontal resolution has the greatest impact on the accuracy of EPV_z. The horizontal resolution of the hydrological measurements and the vertical gradient of the velocity contribute to the uncertainty in EPV_x.

At the rim of the eddy, the isopycnals deviate sharply from the equilibrium depth for the environment waters, creating a horizontal buoyancy gradient. EPV_x is thus large, in contrast to the eddy core where EPV_x is small and EPV_z dominates. This suggests that EPV_x provides a better criterion for eddy boundaries. Note that, without a lateral buoyancy anomaly and without a baroclinic velocity term, EPV_x no longer exists.

Since eddies are stratification anomalies, characterization of the core of the eddy can be achieved using *Ertel Potential Vorticity Anomaly.* The EPV anomaly, ΔEPV, relative to the ocean floor is also used to locate the eddy, compute its volume and characterize its intensity.

The EPV of the ocean at rest (hereafter $\overline{EPV}$) is :

$$\overline{EPV} = f\frac{d\bar{b}}{dz} \tag{11}$$

where $\bar{b}$ is the buoyancy reference profile in the area of the eddy which has been computed as described in part 3.2. The *Ertel Potential Vorticity anomaly* is then calculated on isopycnal surfaces (i.e. using density as a vertical coordinate) as follows:

$$\forall\sigma_0, \quad \Delta EPV(\sigma_0) = EPV(\sigma_0) - \overline{EPV}(\sigma_0) \tag{12}$$

More precisely,

$$\begin{aligned} \forall\sigma_0, \quad \Delta EPV(\sigma_0) &= EPV_x(\sigma_0) + \Delta EPV_z(\sigma_0) && (13) \\ \forall\sigma_0, \quad \Delta EPV_z(\sigma_0) &= EPV_z(\sigma_0) - \overline{EPV}(\sigma_0) && (14) \end{aligned}$$

As for thermohaline anomalies, this quantity is computed on isopycnals surfaces and then represented on geopotential levels. As we can observe in figure 2 panel (i), the boundary of an eddy can be defined by the last closed contour of ΔEPV. With this quantity, both thermohaline anomalies and the velocity field are taken into account. As before, the upper, lower and lateral boundaries of the eddy appear clearly. However, the boundary remains locally defined and highly dependent of the reference profile.

To conclude this section, many diagnostics exist to characterize the core of the eddy and thus calculate its volume (a given isotherm or isohaline, or the total EPV anomaly). Nevertheless, all these criteria depend on an arbitrary reference and are very sensitive to its choice (in particular to compute the eddy volume). In the next section, we propose a criterion to characterize the boundary of an eddy with less arbitrariness.

4 The $\alpha-$criterion for vortex boundary determination

4.1 The $\alpha-$criterion for vortex boundary

In the core of the eddy, EPV_z strongly dominates EPV_x. At its boundary, this dominance becomes less marked due to three combined effects. First, the horizontal buoyancy gradient increases due to cyclo-geostrophic equilibrium; further out, the isopycnals return to the depth of equilibrium for the environment waters. Second, at the boundary, two different water masses meet, creating a frontal region, usually marked by a sizeable horizontal buoyancy gradient. Third, the horizontal shear of the tangential velocity decreases. Peliz et al. (2014) have observed these variations in the EPV component amplitude from a numerical simulation. Here, we use the EPV component amplitude for the first time to characterize the eddy boundary using in-situ data. The EPV_x and EPV_z components of the eddy we studied are shown in figure 2. The core of the eddy is characterized by a homogeneous region of low EPV_z ($EPV_z \approx 2 \times 10^{-10}s^{-3}$) surrounded by a zone where EPV_x is close to $-1 \times 10^{-10}s^{-3}$. Therefore, the eddy boundary can be characterized by the region where the quantity $|EPV_x/EPV_z|$ reach an extremum. To better understand this statement, the modulus of the horizontal and vertical gradients of the two quantities V_o (orthogonal velocity with respect to the ship trajectory) and σ_0 (potential density) are shown in figure 3.

In modulus, the vertical velocity gradient and the horizontal density gradient increase at the boundary of the eddy reaching values of the order of $10^{-3}s^{-1}$ and $10^{-6}kg/m^4$ respectively. On the contrary, the horizontal velocity gradient (or ζ) as well as the vertical density gradient, decrease near the eddy boundary. According to equation (7), this is consistent with EPV_x and EPV_z variations on the eddy boundary. A similar conclusion can be drawn for a cyclonic eddy.

Because in-situ data are sparse, the difference $|EPV_x| - \alpha|EPV_z|$ (where α is a scalar) is less noisy than the ratio $|EPV_x|/|EPV_z|$. Indeed, due to noise, EPV_z can tend to zero in some spurious points making the ratio diverge. We call the criterion α the characterization of the eddy core based on the condition:

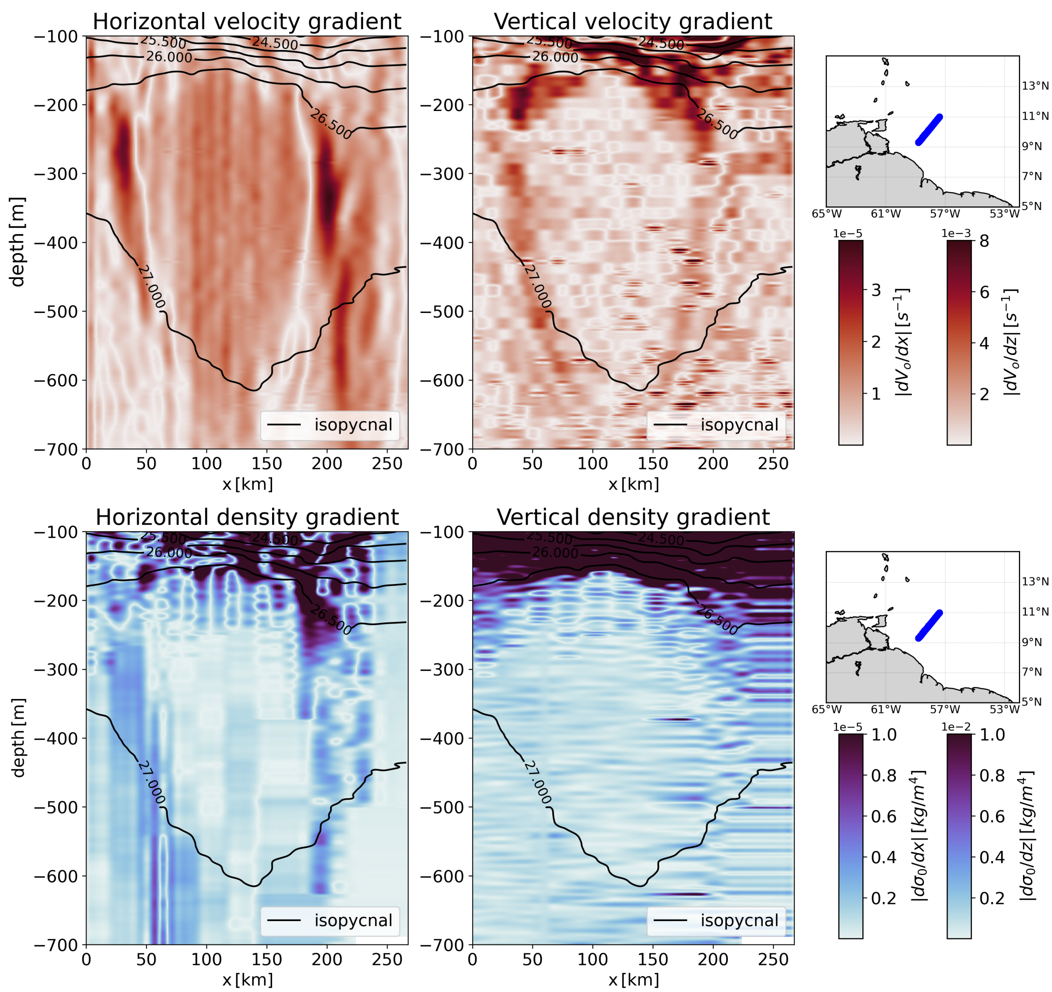

Figure 3. Vertical sections representing the modulus of horizontal and vertical gradients for orthogonal velocity with respect to the ship track V_o and the potential density field σ_0. On the boundary, the modulus of the vertical velocity gradient as well as that of the horizontal density gradient increase. On the contrary, the modulus of horizontal velocity gradient and that of the vertical density gradient decrease. The small geographical maps show where the oceanic eddy has been sampled.

$$|EPV_x| - \alpha|EPV_z| > 0 \tag{15}$$

This approach does not require a reference profile, which is its main advantage over other anomaly-based criteria. An application of this $\alpha-$criterion is shown in figure 4. It maps an area several kilometers wide and the boundary is more irregular than for the point criteria. The upper and lateral boundaries are clear, while the lower boundary is not well defined due to the weak velocity field at this location.

As a consequence, the eddy boundary can be defined as a region whose length scale is comparable with the radius of deformation in one direction but much less than this in the cross direction, across which there are significant changes in buoyancy and velocity with gradients tending to become very large. In fact, this is the definition of a front given by Hoskins (1982) and corroborated by various studies (Voorhis & Hersey, 1964;

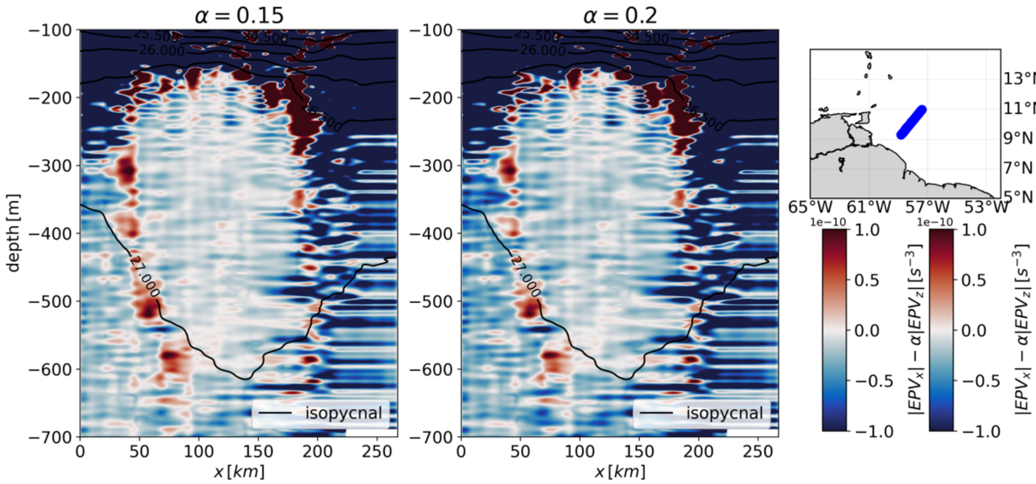

Figure 4. The $\alpha-$ criterion to define the eddy boundary for different thresholds: $\alpha = 0.15$ and $\alpha = 0.2$. This criterion (in dark red) surrounds the core and extends from $10km$ to $50km$. Note that this limit coincides with the inflection points of the isopycnals (see the theoretical part developed in the main text in section 5). The small geographical map shows where the oceanic eddy was sampled.

Katz, 1969; Archer et al., 2020). At the eddy boundary, water recirculates vertically, during frontogenesis or symmetric instability. Indeed, EPV_x and EPV_z are key terms in semi geostrophic frontogenesis (Hoskins & Bretherton, 1972); they drive the dynamics of frontal regions. The associated vertical recirculation tends to flatten isopycnals. This has previously been analysed in numerical simulations (Chen et al., 2020). It has been shown that for high values of EPV_x, instabilities can occur allowing leakages of water masses from the core of the eddy into the environement where it is stirred and mixed.

As a result, the baroclinic components of V_o and the horizontal gradient of σ_0 determine the amplitude of EPV_x with respect to EPV_z. Therefore, the value of α increases with the baroclinicity of mesoscale eddies.

4.2 $\alpha-$criterion validation

In figure 5, we compare all of the previously described criteria we investigated to define mesoscale eddy boundaries for the anticyclone sampled during the EUREC^{4}A-OA field experiment.

We first characterize the eddy core by the value of the EPV anomaly corresponding to the farthest closed contour. This corresponds to $\Delta EPV < -5.10^{-10} s^{-3}$. We also represent the ratio $|EPV_x/EPV_z|$. This region (in dark red) around the core matches well to the $\zeta = 0$ (dark green lines), $\Delta T(\sigma_0) = 0$ and $\Delta S(\sigma_0) = 0$ contours both above the eddy and laterally. Indeed, the thermohaline anomalies and the rotating motion of the eddy are related. Note that, for other eddies, the boundary of the eddy core is best represented by non-zero values of these variables (since the anomalies are computed with respect to a reference profile that may not exactly correspond the water characteristics at the eddy periphery).

The $\alpha-$criterion can thus be related to the eddy thermohaline boundaries $\Delta T(\sigma_0) = 0$ and $\Delta S(\sigma_0) = 0$ and the kinematic boundaries $\zeta = 0$. However, the lateral boundary does not coincide with a simple line corresponding to the $\alpha-$criterion but to a relatively broad zone (reaching $30km$ in some areas). Indeed, it is a region where lateral intrusions and mixing occur (Joyce, 1977, 1984). Moreover, the criterion is less accurate near the base of the eddy because the eddy velocity decreases with depth. Here, the boundary of the eddy seems less pronounced and exchanges of water masses with the surrounding water can take place. In fact, for a given translational velocity of the eddy, as the velocity field decreases with depth, the ability to trap water according to (Flierl, 1981) criterion depends on the depth. In this regards, for the anticyclone we investigate, the base of the eddy seems to be the weakest boundary in terms of exchanges with the environment.

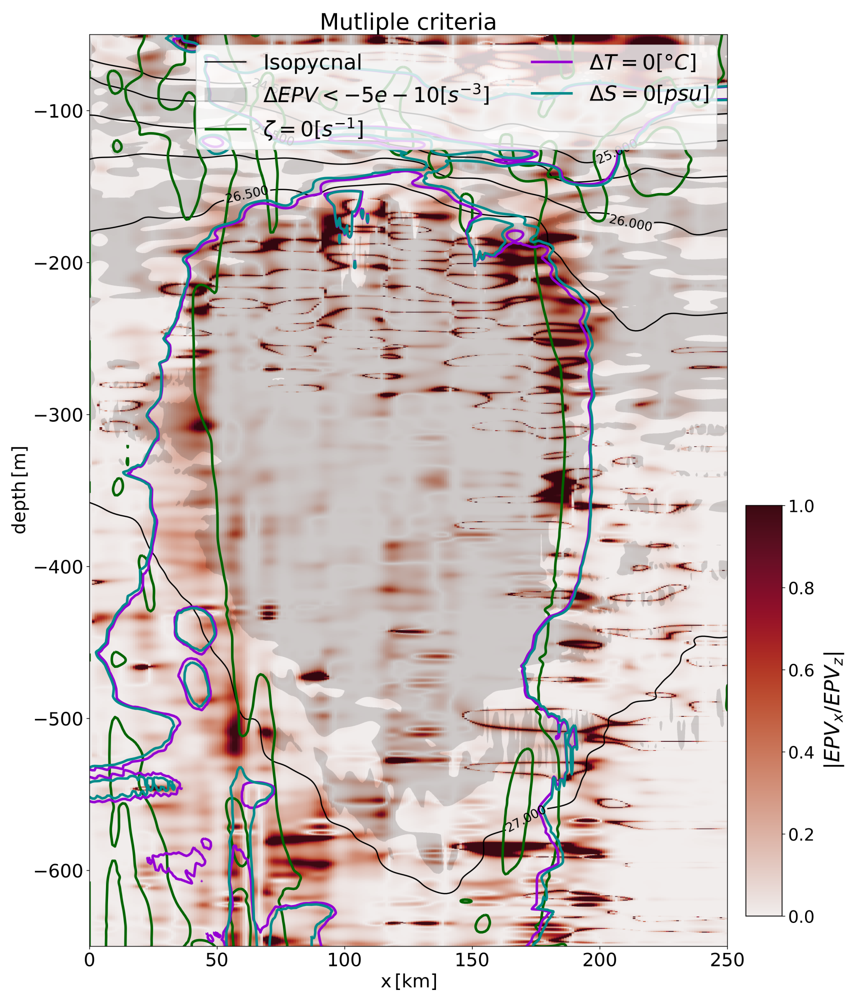

Figure 5. Vertical sections representing the comparison between the possible criteria determining the eddy boundary. In the background, the dark red region corresponds to the α criterion where the ratio EPV_x/EPV_z is directly plotted. The material boundary corresponding to $\Delta T = 0$ and $\Delta S = 0$ are plotted in purple and blue lines. The kinematic boundary corresponding to a change of sign of ζ is represented by a green line. In pale gray, regions where $\Delta EPV < -5 \times 10^{-10} s^{-3}$ have been plotted.

Finally, the upper part of the eddy is well characterized near $200m$ depth, both via the EPV anomaly and via the $\alpha-$criterion. The tropical thermocline (defined by a steep vertical density gradient) is clearly visible at the top of the eddy. Small-scale structures appear between $200m$ and $300m$ depth in the core of the eddy. They correspond to stairslike features in the temperature and salinity profiles (see figure 6). Such features have been commonly observed in the northwest tropical Atlantic by previous studies (Bulters, 2012; Fer et al., 2010). This particular pattern is conserved in the eddy core despite the rotating flow and detected by the $\alpha-$criterion due to strong vertical gradient of buoyancy associated to these strong thermohaline vertical gradient.

We now analyze the interest of the $\alpha-$criterion compared to the previously published Eulerian and Lagrangian criteria. First, many criteria are based on altimetry data which do not give access to the 3D boundary structure. Second, this criterion can be applied to in-situ data, numerical model results, or sea-surface height maps, which allows comparisons. Third, this criterion takes into account both the thermohaline anomaly and the rotating flow, which is not the case for all criteria. Fourth, it represents a way to qualify and quantify the coherence of mesoscale eddies. Indeed, the α value describes the intensity of eddy boundaries. The stronger the thermohaline anomalies, the more intense the boundary. Determining the evolution of α can be interesting to evaluate the temporal variation of the 3D shape of an eddy and its coherence. Fifth, this criterion complements the EPV anomaly criterion; in fact, it determines a boundary region where lateral water mass exchange takes place, rather than a single, well located eddy limit. Since the eddies are constantly responding to the background flow, the isopycnals adjust to this external forcing in the region they evolve. It should also be noted, that this region is close to an inflection point of the isopycnal surfaces.

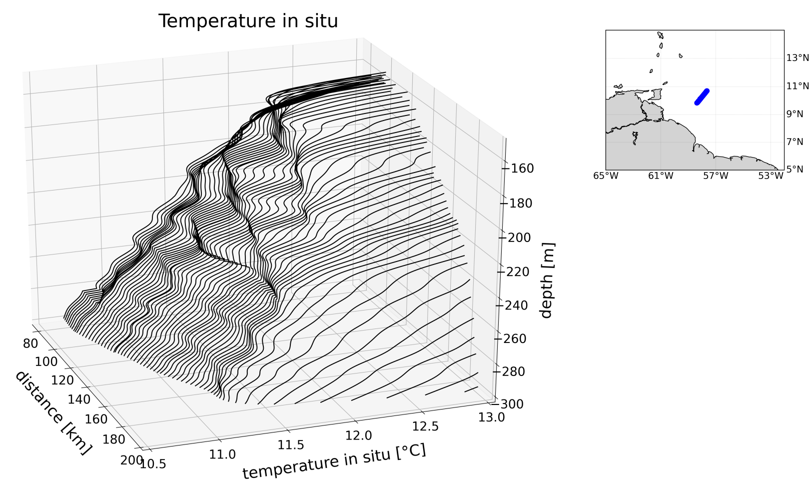

Figure 6. Staircases in the temperature profiles at the top of the subsurface eddy. The x-axis is the same horizontal scale as in figure 1 but it starts at $80km$ for more clarity. Each line is a vertical profile for temperature. Quick variations of these lines create a staircase shape (Bulters, 2012).

4.3 Modeling the vortex profile and estimating the influence of the spatial resolution

The $\alpha-$ criterion is sensitive to the data resolution. In order to study the influence of the data resolution on the results, we developed a simple model. This model has been applied here to the EUREC^{4}A data and more precisely to the anticyclonic eddy of figure 2. The data we use in the model correspond to a vertical section with a resolution in $\vec{x}$ and $\vec{z}$ comparable to those obtained by oceanographic vessels.

First, a generic model has been fitted to the thermohaline anomalies on isopycnal surfaces. In the literature, Gaussian profiles have often been used to model thermohaline anomalies on these surfaces. In our study, a different function better fits the data (derived by using the nonlinear least squares algorithm scipy.optimize.curve_fit in Python). We have then calculated the density anomalies by applying the linearized seawater equation of state in order to use an explicit model equation. Next, we have computed the geostrophic velocity by assuming that the eddy was in geostrophic and hydrostatic equilibrium. Actually, the maximum eddy Rossby number computed using the maximum velocity estimated from the data was 0.61. Nonetheless, for the purpose of this section which is devoted to investigate the sensitivity of the results to the horizontal resolution of the data sampling, the geostrophic approximation is sufficient. Finally, we computed the ratio $|EPV_x/EPV_z|$ from the velocity field and buoyancy anomaly.

This approach can be summarized as follows :

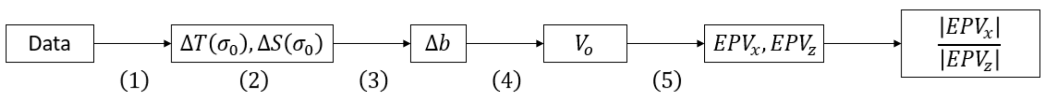

Figure 7. Steps followed: quantities computed at each step are written in boxes

- (1) - A nonlinear least squares algorithm has been used to fit an analytical expression to the data.
- (2) - The formula for the anomaly has been derived as follows: $\Delta a = A_0 \frac{\frac{10}{100\Gamma(0,1)}\exp\left(-\left(\frac{r}{71e3}\right)^{15}\right)}{\max\left(\frac{10}{100\Gamma(0,1)}\exp\left(-\left(\frac{r}{71e3}\right)^{15}\right)\right)}$ with $r^2 = x^2 + (0.25z - 0.25 \times (-400))^2$ locating the center of the anomaly at $(x = 0m, z = -400m)$. The factor 0.25 has been chosen to account for the difference between the horizontal and vertical scales. This formula provides an elliptical pattern for the thermohaline anomaly on the vertical plane. The investigation of more complex functions approximating the anomaly are left for future studies. In the present work, we focused in the optimization by the nonlinear least squares algorithm only the radius $71km$, exponent 15, and center location at $z = -400m$. It should be noted that a value of 15 for the exponent is very rare in the literature. This steepness can be explained when the external flow erodes the rotating flow. In this case, the eddy diffuses less momentum into the background flow (Legras & Dritschel, 1993; Mariotti et al., 1994).
- (3) - the linearized equation of state $\Delta\rho = \rho_0(-\alpha\Delta T + \beta\Delta S - \kappa\Delta P)$ has been used to obtain the density anomaly; α is the coefficient of thermal expansion, β is the coefficient of saline contraction, κ is the isentropic compressibility, ΔT and ΔS are the thermohaline anomalies on isopycnal surfaces, $\Delta p = p - p_{atmospheric} = -\rho_0 g z$ the hydrostatic pressure (we used $\rho_0 = 1026kg/m^3$ as reference density for seawater). The reference values (ρ_0, T_0, S_0) have been calculated using the climatological average in the EUREC^{4}A region.
- (4) - The geostrophic balance $f_0\partial_z V_o = \partial_x \Delta b$ has then been applied with a reference level (no flow condition) $V_o(x, z = -1000m) = 0m/s$. The reference level has been chosen at $-1000m$ in order to lie below the type of eddies we were focusing on (the NBC rings).
- (5) - Formula for EPV. We assume that the Boussinesq approximation and hydrostatic equilibrium hold. We use equation (7).

The temperature anomaly calculated on the isopycnal surfaces is shown in figure 8 panel (a) as an example of step (2). In fact, the model does not fit the data perfectly. There are several possible reasons for this: the geostrophic balance is not accurate near the peak of the tangential velocity, where cyclostrophic effects are not negligible. The eddy background is not modeled here, in particular the tropical thermocline which causes the velocity field to decrease rapidly in the upper layers. The fields in the model are assumed to be stationary whereas they are not in reality. Finally, the f-plane approximation is used whereas, for large eddies, the $\beta-$plane approximation would be more appropriate. For information, the steepness of the radial temperature (or salinity) profile can be explained by shear effects that may have stripped the outer layers of the eddy. Regardless, the quantities provided by the model (see panels (b), (c), (d) and (e)) seem reasonably consistent with the data: V_o seems quite faithfull and EPV_x increases at the boundaries as does the ratio $|EPV_x/EPV_z|$. The latter follows the region where the horizontal buoyancy gradient is large, which is the case in the observed anticyclonic eddy. The shape of the eddy as well as the orders of magnitude of the anomalies are consistent with the observed eddy properties.

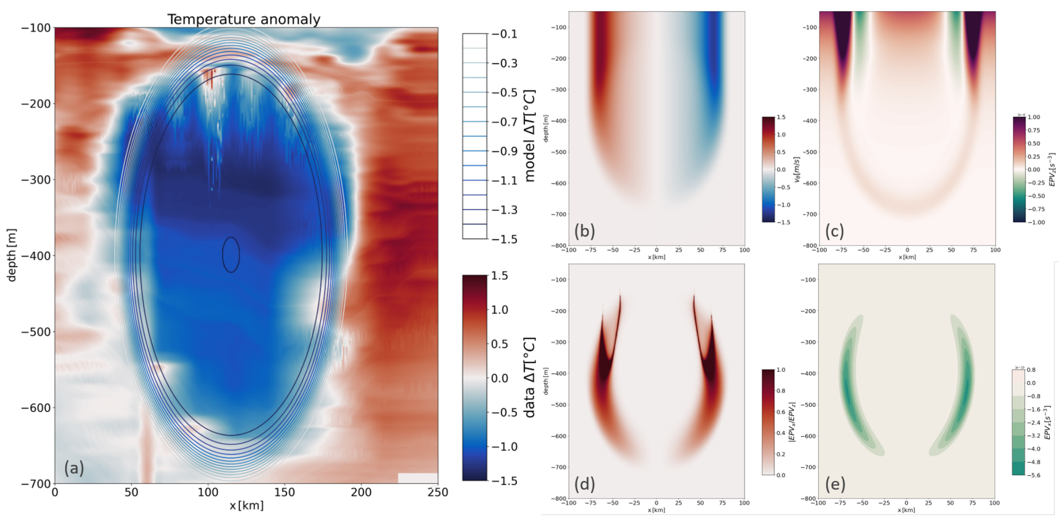

Figure 8. Vertical sections for the modelled anticyclonic eddy. (a) comparison between data and model profile for the temperature anomaly, contours of constant value for the model are plotted. Fitting the gradient of anomalies directly impacts the EPV computation and thus the $\alpha-$boundary. (b) azimuthal velocity for the model which reach a maximum value at the sea surface. (c) ratio $|EPV_x/EPV_z|$, (d) EPV_x, (e) EPV_z for the model.

To evaluate the impact of spatial resolution on the $\alpha-$criterion, we calculated, as a reference, a vertical section with a very high resolution ($\Delta x = 100m, \Delta z = 0.1m$). Other sections were subsequently computed with lower spatial resolutions. As shown in figure 1, the ratio $|EPV_x/EPV_z|$ diverges in the upper part of the eddy, near $300m$ depth. This divergence is obviously not present in the observed eddy, which underlines the limits of the model. Thus, to calculate the difference between the high-spatial resolution reference section and sections at lower resolution, we only consider the lower part of the eddy at depths ranging from $400m$ to $1000m$.

With this assumption, the reference EPV ratio $Ra = |EPV_x/EPV_z|$ reaches its maximum of 1.342 at $z = -400m$ and $r = \pm 59km$. Maximal error as well as maximal RMS between a lower resolution profile and the reference profile are plotted to analyse the impact of resolution. The maximum error is defined as $e_{max} = max|Ra_{ref} - Ra|, r \in [-100; 100], z \in [-1000; -400]$. Results are shown in figure 9.

This figure shows that the lower the resolution, the higher is the error. The horizontal resolution mainly influences the accuracy of the results. The vertical resolution has less influence on the maximum error and RMS. Even in the case of the relatively high horizontal resolution ($10km$) of the EUREC4A data, the maximum error is 0.8 or 58% of the maximum value of Ra. The resolution largely constrains the accuracy of the results. However, the shape of the eddy boundary appears to be less sensitive to resolution. For instance, for a horizontal resolution of $10km$, the RMS is 0.21 or 16% of the maximum Ra. Moreover, in-situ data are often affected by noise not taken into account here. In conclusion, the resolution has a high impact on the quantitative values of the criteria but a moderate impact on the shape of the eddy boundary.

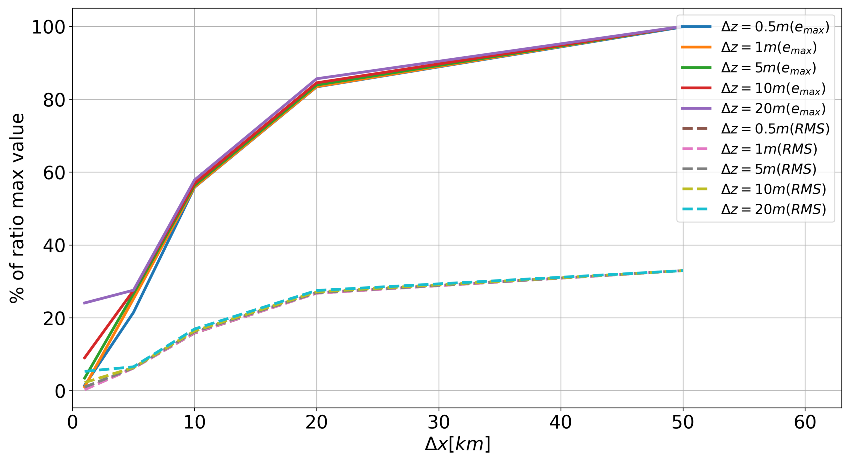

Figure 9. Maximum RMS and maximum error, in percentage of the ratio maximum value, as a function of horizontal resolution. Curves are plotted for various value of Δz.

4.4 A generic method to compare eddy boundaries

In this section, the $\alpha-$criterion is used to compare the intensity of eddy boundaries. We describe the methodology for a single eddy. The boundary of this eddy is characterized by the $\alpha-$criterion as detailed previously. The value of α denotes the intensity of the boundary. To quantify the intensity of the boundary, we computed its area A_α in the $(\vec{x}, \vec{z})$ plane numerically. Obviously, the higher α is, the smaller the surface of the boundary is: A_α is a decreasing function of α. α will reach higher values over a greater proportion of the total frontier area of the eddy for a more intense eddy boundary. In that case, A_α will decrease more slowly. What influences the intensity of the boundary is investigated in the theoretical part. To compare the curves, A_α is arbitrarily normalized by $A_{0.01}$. Finally, the curves are plotted on the same figure (10) for $\alpha \geq 0.01$ in order to compare the intensity of the boundary with respect to the boundary zone.

To compute A_α on the grid $(\vec{x}, \vec{z})$ with a given resolution $(\Delta x, \Delta z)$, each point of the grid satisfying $|EPV_x| - \alpha|EPV_z| > 0$ is selected. The number of points is noted N and $A_\alpha = N \times \Delta x \times \Delta z$. This process is repeated for several values of α and, after normalization, we obtain figure 10. It should be noted that the boundary region corresponds to a volume in space. Here, with 2D fields, only a section of this volume can be observed. Moreover, the numerical values obtained here are not perfectly accurate but they provide orders of magnitude.

In black, the result is plotted for the model described in section 4.3 (with very high resolution $\Delta x = 100m$ and $\Delta z = 0.1m$), as well as the curve for the subsurface eddy in figure 2. For small values of α, the boundary is less marked in the model. This is because the boundary is considerably better defined in space in the model and depends directly on the analytical derivative of the thermohaline anomalies shape.

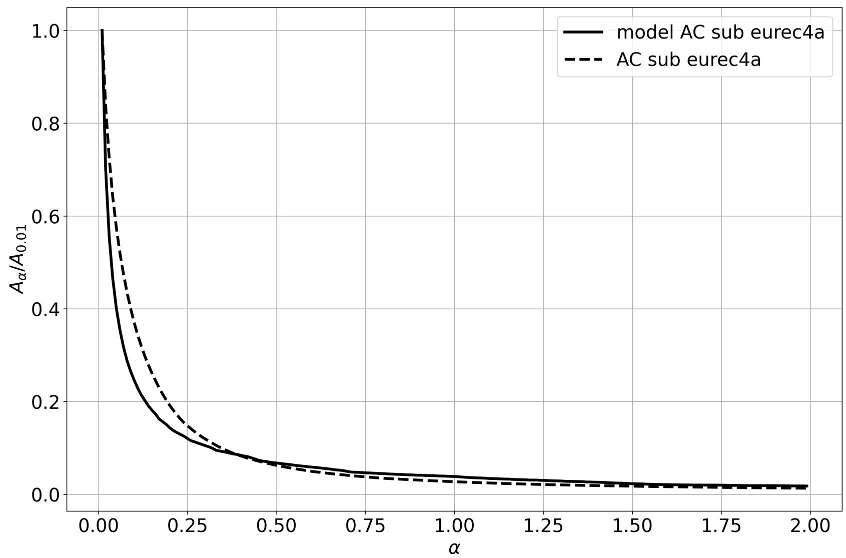

Figure 10. Intensity of eddy boundaries : comparison between data (dashed line) and model (continuous line). The ordinate axis represents the normalized boundary. The abscissa axis is showing the value taken by α.

For large values of α, the boundary is wider in the model showing that the model more effectively highlights areas of high intensity. Indeed, the resolution in the model is much higher than in the observations. It should also be recalled that the ageostrophic component of the velocity field has been neglected in the model and that the background stratification that constrains the α values is not taken into account.

This method seems to provide robust results and may be used in future to assess the coherence of mesoscale eddies. Indeed, when an eddy boundary weakens due to the interaction with topography or in presence of external shear flows, its boundary is eroded and thus $\int^{\alpha} A(\alpha')/A_{0.01} d\alpha'$ decreases.

4.5 A subsequent criterion : comparison between ΔEPV_z and EPV_x

Using the same idea, since EPV_x is stronger at the eddy boundary (Yanxu, 2022; Zhang, 2014 (Zhang et al., 2014)), the ratio $|\Delta EPV_z/EPV_x|$ can be used to separate the eddy core from its boundary.

Figure 11 shows that $|\Delta EPV_z/EPV_x| > \beta$, with $\beta = 50$ in the core of the anticyclonic eddy, decreases to a ratio of 5 or less at the edge of the eddy. The value of 50 was chosen to obtain the last closed contour of $|\Delta EPV_z/EPV_x|$ from the eddy center. Therefore, the EPV anomaly in the eddy cores is mainly due to the EPV_z term. As the EPV anomaly is due to the anomaly in stratification and relative vorticity, the influence of the EPV_x term becomes significant only at the eddy boundary. This coincides with the results previously obtained on the ratio $|EPV_x/EPV_z|$. To our knowledge, this calculation has never been performed on in-situ data. Previous studies have neglected the EPV_x term in the EPV anomaly (e.g., Paillet et al., 2002) because it only slightly modifies the wavy shape of the boundary. In fact, this term highlights and quantifies the frontability of the turbulent eddy boundary.

A drawback of this criterion is that it also detects regions where $\Delta EPV_z > EPV_x$ outside the core of the eddy. Therefore, one must assume the connectedness of the core to eliminate these outlying regions. Finally, note that the lower boundary of the eddy is more evident with this criterion. Following the last closed contour, the base of this anticyclone is located near $z = -650m$.

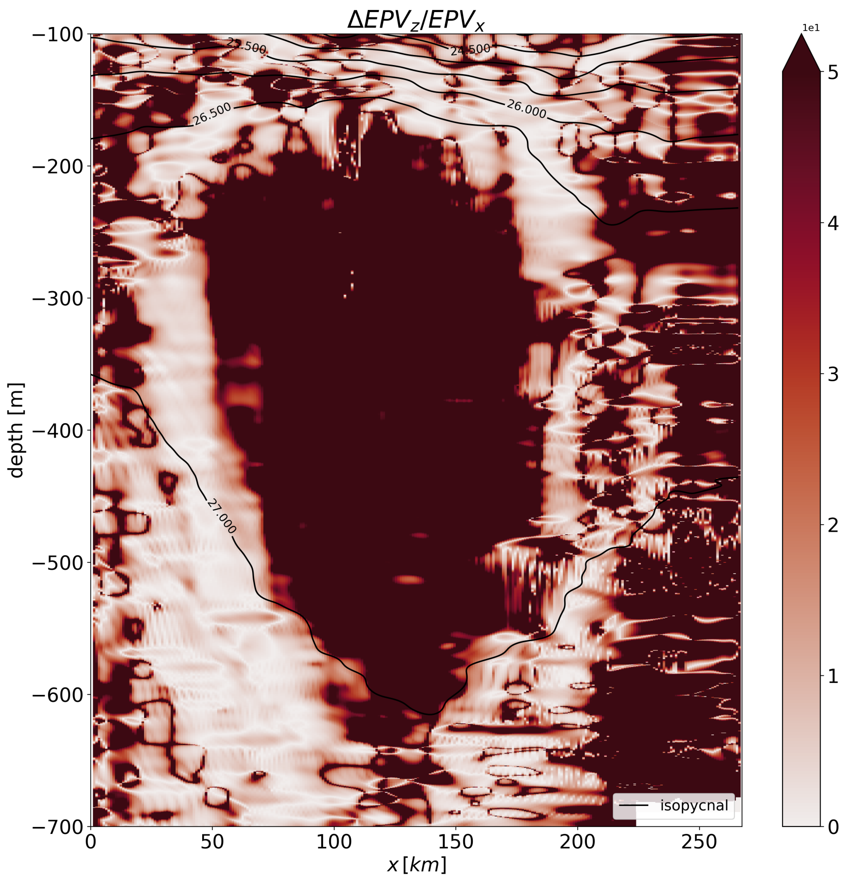

Figure 11. Vertical section representing the modulus of the ratio between ΔEPV_z and EPV_x ; Colors have been saturated in order to obtain an homogeneous core. The clear boundary represents the region where the baroclinic term EPV_x has a non negligible value compare to ΔEPV_z.

5 Theoretical aspects and discussion

5.1 $\alpha-$criterion for a generic eddy

The objective of this section is to apply the criterion to a generic eddy in an otherwise quiescent idealized ocean. Our goal is to illustrate the criterion and to find orders of magnitude for the α values. Consider an isolated and stable circular eddy near the surface of a continuously stratified ocean. We assume the $f-$ plane approximation ($f = f_0$). Assume that this eddy traps water in its core, so that the density field ρ can be decomposed into cylindrical coordinates as follows:

$$\rho(r,z) = \overline{\rho}(z) + \rho'(r,z) \tag{16}$$

$$\overline{\rho}(z) = \rho_w + \rho_1 e^{z/D} \tag{17}$$

$$\rho'(r,z) = \rho_0 e^{z/H} e^{-r^\delta/R^\delta} \tag{18}$$

$\overline{\rho}(z)$ is the stratification of a quiescent ocean composed of $\rho_w = 1000kg/m^3$ the water density, ρ_1 the surface density anomaly relative to ρ_w, and D the vertical scale of the undisturbed stratification. The perturbed density profile adds an exponential power anomaly of amplitude ρ_0 and steepness δ (Carton et al., 1989). The characteristic radius of the profile is noted R. This anomaly decreases exponentially in the vertical direction on a scale H. Assuming that the eddy is in hydrostatic and geostrophic equilibrium, the velocity field v_θ, the pressure anomaly p' and the density anomaly ρ' are related by the following equations:

$$\begin{aligned} f_0 v_\theta &= \frac{1}{\rho_w}\frac{\partial p'}{\partial r} && (19)\\ \frac{\partial p'}{\partial z} &= -g\rho' && (20)\end{aligned}$$

As for the model, only the geostrophic component of velocity is computed by simplicity but, as we saw, the eddy Rossby number may not be small. Injecting the expression of ρ' into these equations and computing pressure and velocity leads to :

$$\begin{aligned} p'(r,z) &= p_0 e^{z/H} e^{-r^\delta/R^\delta} && (21)\\ v_\theta(r,z) &= V_0\left(\frac{r^{\delta-1}}{R^{\delta-1}}\right) e^{z/H} e^{-r^\delta/R^\delta} && (22)\end{aligned}$$

with $p_0 = -\rho_0 g H$ and $V_0 = \frac{-\delta p_0}{f_0 \rho_w R}$. The relative vorticity can also be computed with the velocity field and we introduce the buoyancy field :

$$\begin{aligned} \zeta(r,z) &= \frac{\delta V_0}{R}\left(\frac{r^{\delta-2}}{R^{\delta-2}}\right)\left(1-\frac{r^\delta}{R^\delta}\right) e^{z/H} e^{-r^\delta/R^\delta} && (23)\\ b(r,z) &= -g\frac{\rho}{\rho_w} && (24)\end{aligned}$$

In order to find variations of α as well as an order of magnitude, each quantity is normalized. We therefore introduce the normalized variables $\overline{r} = r/R$ and $\overline{z} = z/H$, the normalized quantities $\overline{b} = b/g$, $\overline{v_\theta} = v_\theta/V_0$ and $\overline{\zeta} = \zeta/(\delta V_0/R)$, and the parameters $\xi = H/D$, $\gamma = \rho_1/\rho_0$. We then obtain:

$$\begin{aligned} \overline{b}(r,z) &= -1 - \frac{\rho_0}{\rho_w}\left(\gamma e^{\xi\overline{z}} + e^{\overline{z}} e^{-\overline{r}^\delta}\right) && (25)\\ \overline{v_\theta}(r,z) &= \overline{r}^{\delta-1} e^{\overline{z}} e^{-\overline{r}^\delta} && (26)\\ \overline{\zeta}(r,z) &= \overline{r}^{\delta-2}\left(1-\overline{r}^\delta\right) e^{\overline{z}} e^{-\overline{r}^\delta} && (27)\end{aligned}$$

ξ represents the influence of the perturbed stratification relative to that of the quiescent ocean. γ introduces the influence of the amplitude of the density anomaly generated by the trapped water relative to the amplitude of the density of the ocean at rest. For an axisymmetric eddy on the $f-$ plane, the Ertel potential vorticity is written as follows:

$$q = q_r + q_z = -\frac{\partial v_\theta}{\partial z}\frac{\partial b}{\partial r} + (\zeta + f_0)\frac{\partial b}{\partial z} \qquad (28)$$

We normalize these quantities by $gV_0/(HR)$ and compute the ratio $\mathbf{R} = q_r/q_z$ using the normalized quantities previously introduced, so that:

$$\begin{aligned} \mathbf{R} &= \frac{q_r}{q_z} = \frac{\overline{q_{\overline{r}}}}{\overline{q_{\overline{z}}}} && (29)\\ &= \frac{-\delta^2 R_o\left(\overline{r}^{\delta-1} e^{\overline{z}} e^{-\overline{r}^\delta}\right)^2}{\left(\delta R_o \overline{r}^{\delta-2}\left(1-\overline{r}^\delta\right) e^{\overline{z}} e^{-\overline{r}^\delta} + 1\right)\left(\gamma\xi e^{\xi\overline{z}} + e^{\overline{z}} e^{-\overline{r}^\delta}\right)} && (30)\end{aligned}$$

where $R_o = \frac{V_0}{f_0 R}$ is the Rossby number. Equation (30) is the complete analytical expression for the limit of this generic surface eddy described by the $\alpha-$criterion. When, $\overline{r}$ tends to 0, $\mathbf{R}$ also tends to 0; this is consistent with the results obtained with the EUREC^{4}A-OA observations. However, the most interesting parameter is the limit of the eddy, mathematically when $\overline{r}$ tends to 1. Note that the denominator is a strictly positive regular function and that $\mathbf{R}$ is defined for all $\overline{r}. \in \mathbf{R}$ and for all $\overline{z} \in]-\infty;0]$. In particular:

$$\begin{aligned} \mathbf{R}(\overline{r}=1,\overline{z}) &= \frac{-\delta^2 R_o}{F_{\xi,\gamma}(\overline{z})} && (31) \\ F_{\xi,\gamma}(\overline{z}) &= \gamma\xi e^{\overline{z}(\xi-2)-2} + e^{1-\overline{z}} && (32) \end{aligned}$$

As before, the denominator $F_{xi,\gamma}$ is strictly positive, regular and it diverges when *overlinez* tends to $-\infty$. As indicated above, $\mathbf{R}$ is negative. Note that the limits of the eddy depend on the square of the slope of the velocity field, the Rossby number, the magnitude of the buoyancy anomaly, and the ratio between the two characteristic length scales of the stratification (at rest and perturbed). The larger ρ_0 is compared to ρ_1, the larger $\mathbf{R}$ will be. And the more the isopycnes are spaced, the smaller H is with respect to D and the larger $\mathbf{R}$ is. This dependence is interesting because these terms are related to the baroclinicity of the eddy (related to the slope of the eddy velocity and the deviation from the background stratification due to the presence of the eddy) and to the nonlinearity of the velocity field. These properties determine the strength of the eddy boundaries (in terms of permeability of water exchanges and dissipation) and thus control the cohesiveness or coherence of the eddy.

Taking into account the regularity of the denominator, $\mathbf{R}$ is bounded and:

$$|\mathbf{R}(\overline{r}=1,\overline{z})| \leq \frac{\delta^2 R_o}{\min_{]-\infty;0]} F_{\xi,\gamma}(\overline{z})} \tag{33}$$

A more thorough study of the denominator shows that for $\xi \leq 2$, its derivative with respect to $\overline{z}$ is negative and, consequently, $F_{\xi,\gamma}$ decreases on $]-\infty;0]$ to reach its minimum at $\overline{z}=0$, i.e. at the surface. In this case, the upper limit given by equation (33) is $\frac{\delta^2 R_o}{\gamma\xi e^{-2}+e}$. The influence of the density anomaly parameters is clearly visible in this expression. For $\xi > 2$, $F_{\xi,\gamma}$ decreases on $]-\infty;\overline{z}_0]$ to reach a minimum at $\overline{z}_0 = \frac{3-\ln\gamma\xi(\xi-2)}{\xi-1}$. We can show that this quantity is always negative regardless of the value of γ.

In the literature, ξ depends on the ocean basin and the type of eddy but an order of magnitude between 1.5 and 3 is quoted. In the case where $\xi = 3$, two isopycnals initially $50m$ apart are now $150m$ apart in the perturbed stratification. In parallel, ρ_0 and ρ_1 also depend on the type of eddy and on the ocean basin. However, for the anticyclonic eddy studied here, ρ_1 is $26kg/m^3$ while ρ_0 is $0.1kg/m^3$ (see figure 2 panel (c)), which means that γ is 260. Taking, $\delta = 15$ (see the model in Section 4.3), $\gamma = 260$, $\xi = 2$ and $R_o = 0.6$, we obtain $\mathbf{R}(\overline{r}=1,\overline{z}) \leq 1.9$. This value is consistent with figure 10 where 99% of the surface is characterized by a value of α less than 2.

5.2 Curvature of isopycnals

In this section, we provide a geometric interpretation of the $\alpha-$criterion. In figure 4, the boundaries of the vortices appear to coincide vertically with the inflection points of the isopycnals. Using theoretical considerations, we try to find out when this coincidence is verified.

Consider an isopycnal surface vertically displaced by the presence of an oceanic eddy in the $f-$ plane. On this isopycnal surface, the variations of the b field are zero, so:

$$db = \frac{\partial b}{\partial r}dr + \frac{\partial b}{\partial z}dz = 0 \tag{34}$$

Let us note z_b the geopotential level of this isopycnal of value b. By definition, its variation with respect to r depends on horizontal and vertical gradients such that :

$$\frac{dz_b}{dr} = \frac{-\partial b/\partial r}{\partial b/\partial z} \tag{35}$$

Searching for an inflexion point leads to the following condition :

$$\frac{d^2 z_b}{dr^2} = \frac{1}{\partial b/\partial z}\left(-\frac{\partial^2 b}{\partial r^2} + \frac{\partial b}{\partial r}\frac{\partial^2 b/\partial z^2}{\partial b/\partial z}\right) = 0 \tag{36}$$

which can be re-written :

$$\frac{\partial^2 b}{\partial r^2}\frac{\partial b}{\partial z} = \frac{\partial^2 b}{\partial r \partial z}\frac{\partial b}{\partial r} \tag{37}$$

Assuming that the vortex is in geostrophic equilibrium, the radial buoyancy gradient can be expressed as a function of the velocity gradient using the thermal wind equation:

$$\frac{\partial^2 b}{\partial r^2} = f_0 \frac{\partial^2 v_\theta}{\partial r \partial z} \tag{38}$$

$$\frac{\partial^2 b}{\partial r \partial z} = f_0 \frac{\partial^2 v_\theta}{\partial z^2} \tag{39}$$

Re-injecting those expressions in equation (37) leads to:

$$\frac{\partial^2 v_\theta}{\partial r \partial z}\frac{\partial b}{\partial z} = \frac{\partial^2 v_\theta}{\partial z^2}\frac{\partial b}{\partial r} \tag{40}$$

This reflects the link between the buoyancy field and the velocity field at an inflection point.

Now, we can apply the $\alpha-$criterion. On the $\alpha-$boundary of the eddy, we have:

$$|q_r| - \alpha|q_z| \geq 0 \tag{41}$$

which can be simplified because $\zeta \approx 0$ at the boundary. Developing equation (41), the buoyancy and velocity fields are linked by:

$$|\frac{\partial v_\theta}{\partial z}\frac{\partial b}{\partial r}| \geq |\alpha f_0 \frac{\partial b}{\partial z}| \tag{42}$$

Then, we can compute the ratio between equations (40) and (42), which leads to:

$$|\frac{\partial^2 v_\theta/\partial z^2}{\partial v_\theta/\partial z}| \leq |\frac{\partial^2 v_\theta/\partial r \partial z}{\alpha f_0}| \tag{43}$$

As in the previous section, let us introduce the scales associated with each quantity: H for z, V_0 for v_θ and R for r. In order of magnitude, the isopycnal curvature corresponds to $\alpha-$criterion in regions where:

$$\alpha \leq R_o \tag{44}$$

where R_o is the Rossby number. We find the result of the previous section when it was shown that the ratio $\mathbf{R}$ was a linear function of R_o. For the subsurface anticyclonic eddy of figure 2, figure 10 showed that 95% of the boundary zone was characterized by a α lower than 0.75 which is consistent with a maximum Rossby number of 0.61.

6 Conclusion

Observations collected during the international field experiment EUREC4A-OA show that the North Brazilian Current rings are ocean eddies bounded in space by a well-defined frontal region. Several criteria have been used in published studies to characterize this region. However, they have either found a point boundary or relied greatly on reference values *a priori*. In this study, we propose a new criterion based on Ertel potential vorticity to characterize the boundaries of the eddy, including its upper and lower edges. This criterion compares the vertical and horizontal components of the Ertel potential vorticity. The eddy boundary is characterized by a relatively intense horizontal component of the EPV. When applied, the threshold on this component identifies a relatively broad region instead of a well-defined point boundary. The limited width of this region imply that local turbulent process are at play while they have a limited impact on water mass exchange and mixing. The boundary or frontal zone of the eddy is also characterized by steep isopycnic slopes and a baroclinic velocity field.

Using a generic anticyclonic eddy, we show that the relative intensity of the horizontal component to the vertical component of the EPV depends on the slope of the velocity field, the Rossby number and the vertical stratification anomaly. This criterion ("relative intensity equal to the α threshold") coincides with the inflection points of isopycnal surfaces when α is of order R_o. These results suggest that the strength of the eddy boundaries and thus the ability of the eddy to remain coherent and not dissipate are governed by the baroclinicity of the eddy, the level of ageostrophy, and the intensity of the anomaly on the vertical stratification. In future work this will need to be studied in more detail to assess the robustness and generalizability of these results.

This study also highlights the critical importance of not only vertical, but also horizontal high-resolution spatial sampling of the thermohaline and velocity eddy properties. This is necessary to minimize errors in the criterion estimation as well as in the identification of the eddy boundaries. To obtain more information on the nature of mesoscale ocean dynamics, we therefore recommend that future oceanographic surveys adequately de sampling distance between vertical profiles when measuring these structures. This recommendation also applies to the spatial resolution of numerical models.

In conclusion, future work should verify the validity and applicability of the α criterion we have defined by analyzing other mesoscale ocean eddies that are well resolved in terms of observations and numerical simulations. Comparisons with Eulerian and Lagrangian criteria are also needed to better understand and characterize eddy coherence and the different processes that control it.

Acknowledgments
This research has been supported by the European Union's Horizon 2020 research 893 and innovation program under grant agreements no. 817578 (TRIATLAS), the Centre National d'Etudes Spatiales through the TOEddies and EUREC4A-OA projects, the French national programme LEFE INSU, IFREMER, the French vessel research fleet, the French research infrastructures AERIS and ODATIS, IPSL, the Chaire Chanel programme of the Geosciences Department at ENS, and the EUREC4A-OA JPI Ocean and Climate

programme. We also warmly thank the captain and crew of RVs Atalante and Maria S. Merian. Yan Barabinot is supported by a Ph.D grant from Ecole Normale Supeerieure de Saclay. Xavier Carton acknowledges support by UBO and by a CNES contract EUREC4A-OA. The in-situ data were processed by Dr Pierre L'Hegaret (LMD/ENS).

Appendix A The semi-geostrophic Charney-Stern criterion and a restriction of α values

In the previous part, it was shown that the intensity of an eddy boundary was dependant on the Rossby number, the steepness of the velocity field and the buoyancy anomaly. Therefore, α is mostly smaller than unity. However, one can wonder whether an upper bound can be found to α values. In this part, we use the semi-geostrophic Charney-Stern criterion for vortex instability with a focus on the eddy boundary to find an upper bound for α values.

Indeed, as mentionned above, at the eddy boundary, water recirculates vertically, during frontogenesis or symmetric instability and EPV_x and EPV_z are key terms in semi geostrophic frontogenesis (Hoskins & Bretherton, 1972).

Here, we follow the Kushner and Shepherd (1995) approach, to derive a semi-geostrophic Charney-Stern criterion for an isolated vortex on the $f-$plane. initially, we tried to adapt the Kushner and Shepherd (1995) theory in cylindrical coordinates adding the cyclostrophic term to the equations. However, in polar coordinates, the radial and orthoradial velocity components are not independent due to the radius of curvature r. Especially, $v_\theta = r\dot{\theta}$ cannot be reduced to a generalised coordinate as in the Cartesian case due to this $r-$dependence. As a consequence, further assumptions were needed.

As in part 5.1, consider an isolated but not necessarily axisymmetric eddy, at the surface of an infinite ocean. The radius of maximum velocity is denoted R and the generic velocity field takes the following form :

$$\vec{v}(r,\theta,z,t) = v_r(r,\theta,z,t)\vec{e_r} + v_\theta(r,\theta,z,t)\vec{e_\theta} + v_z(r,\theta,z,t)\vec{e_z} \tag{A1}$$

In cylindrical coordinates, the flow is governed by the following equations :

$$\begin{aligned}
\frac{Dv_r}{Dt} - (f_0 + \frac{v_\theta}{r})v_\theta &= -f_0 v_\theta^g && \text{(A2)}\\
\frac{Dv_\theta}{Dt} + (f_0 + \frac{v_\theta}{r})v_r &= f_0 v_r^g && \text{(A3)}\\
\frac{1}{\rho_w}\frac{\partial p'}{\partial z} &= b' && \text{(A4)}\\
\frac{1}{r}\frac{\partial (r v_r)}{\partial r} + \frac{1}{r}\frac{\partial v_\theta}{\partial \theta} + \frac{\partial v_z}{\partial z} &= 0 && \text{(A5)}\\
\frac{Db'}{Dt} &= 0 && \text{(A6)}\\
\frac{D}{Dt} &= \frac{\partial}{\partial t} + v_r\frac{\partial}{\partial r} + v_\theta\frac{\partial}{r\partial \theta} + v_z\frac{\partial}{\partial z} && \text{(A7)}
\end{aligned}$$

where, v_r^g and v_θ^g are the geostrophic velocity respectively in the radial and orthoradial directions. As previously, the prime denotes the buoyancy anomaly associated to the trapped water mass in the eddy core. As instabilities develop locally and R is very large, we assume that the flow can be described in a local Cartesian frame near the eddy boundary (see figure A1). As we study small variations of r closed to R, we define the Cartesian variable $\varepsilon = r - R$ with $\varepsilon \ll R$. The curvature is locally neglected and we define the second Cartesian variable $y = R\theta$. Consequently, the local Cartesian frame $(\vec{e}_\varepsilon, \vec{e}_y, \vec{e}_z)$ and the associated velocity field $\vec{v}(\varepsilon, y, z, t)$ are defined. Moreover, let us define the rotating speed $\Omega = \frac{v_\theta}{r}$ in the cylindrical system which leads to $\Omega_R(\varepsilon, y, z, t)$

in the local Cartesian frame. Note that Ω_R is a regular function of ε because it cannot diverge close to the eddy center nor at infinity. Then, it exists a potential χ such that $\frac{d\chi}{d\varepsilon} = \Omega_R$. It will help us defining the generalized coordinates.

In this frame of reference, equations simply write :

$$
\begin{aligned}
\frac{Dv_\varepsilon}{Dt} - (f_0 + \Omega_R) v_y &= -f_0 v_y^g && \text{(A8)}\\
\frac{Dv_y}{Dt} + (f_0 + \Omega_R) v_\varepsilon &= f_0 v_\varepsilon^g && \text{(A9)}\\
\frac{1}{\rho_w}\frac{\partial p'}{\partial z} &= b' && \text{(A10)}\\
\frac{\partial v_\varepsilon}{\partial \varepsilon} + \frac{\partial v_y}{\partial y} + \frac{\partial v_z}{\partial z} &= 0 && \text{(A11)}\\
\frac{Db'}{Dt} &= 0 && \text{(A12)}\\
\frac{D}{Dt} &= \frac{\partial}{\partial t} + v_\varepsilon \frac{\partial}{\partial \varepsilon} + v_y \frac{\partial}{\partial y} + v_z \frac{\partial}{\partial z} && \text{(A13)}
\end{aligned}
$$

Note that this system is quite particular because cyclostrophic terms have been kept whereas the local curvature is small, but they are necessary for the global analysis.

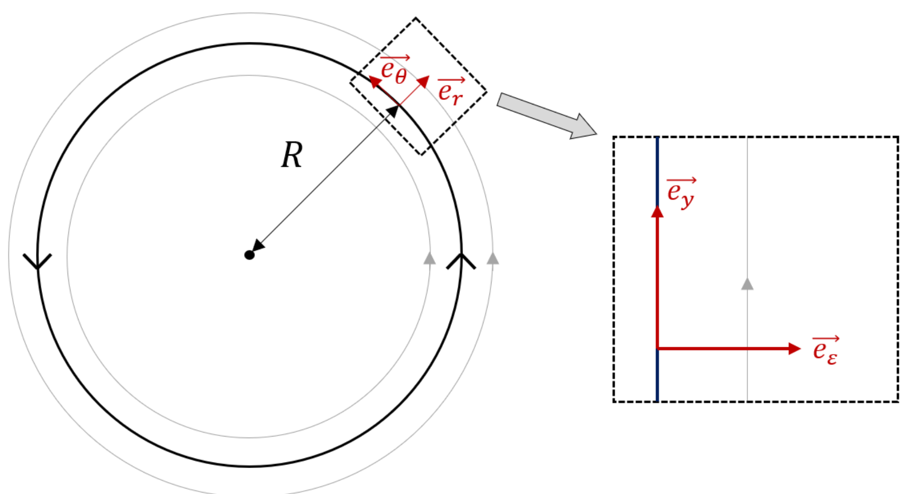

Figure A1. Local Cartesian frame at the eddy boundary. The curvature is locally neglected

Following Kushner and Shepherd (1995), we define the generalized coordinates, $T = t$, $E = \varepsilon + \frac{v_y}{f_0} + \frac{\chi}{f_0}$, $Y = y - \frac{v_\varepsilon}{f_0} + y\frac{\Omega_R^{(0)}}{f_0}$ and $Z = \frac{b'}{f_0^2}$ such that :

$$
\begin{aligned}
\frac{DY}{Dt} &= v_y && \text{(A14)}\\
\frac{DE}{Dt} &= v_\varepsilon && \text{(A15)}\\
\frac{DZ}{Dt} &= 0 && \text{(A16)}
\end{aligned}
$$

In fact, we replaced Ω_R by its constant value $\Omega_R^{(0)}$ at $\varepsilon = 0$ and at $t = 0$. When t is large, the Y variable is incomplete because of the cyclostrophic term, thus we cannot obtain the desired form of the problem. To the best of our knowledge, a generalized system of coordinates has never been found in cylindrical coordinates due to this cyclostrophic term. Even if this change of variable is incomplete, it will not change the stability criterion as the base flow is oriented according to $\vec{e_y}$ in our Cartesian frame. Then, the Montgomery-Bernoulli potential for the local frame can be defined as a function of the pressure p and velocities such that :

$$\Psi = \frac{p}{\rho_0} - f_0^2 Zz + \frac{1}{2}(v_\varepsilon^2 + v_y^2) \tag{A17}$$

which gives,

$$v_\varepsilon = -\frac{1}{f_0}\frac{\partial \Psi}{\partial Y} \tag{A18}$$

$$v_y = \frac{1}{f_0}\frac{\partial \Psi}{\partial E} \tag{A19}$$

The material derivative can also be expressed using these variables :

$$\frac{D}{DT} = \frac{D}{Dt} = \frac{\partial}{\partial T} - \frac{1}{f_0}\frac{\partial \Psi}{\partial Y}\frac{\partial}{\partial E} + \frac{1}{f_0}\frac{\partial \Psi}{\partial E}\frac{\partial}{\partial Y} \tag{A20}$$

Then, the Jacobian of the transformation is proportional to the Ertel Potential vorticity q of the flow :

$$q \propto \frac{\partial(E, Y, Z)}{\partial(\varepsilon, y, z)} \tag{A21}$$

For a frontal vortex, we use the inverse of this quantity is relevant to avoid isopycnal pinching. We denote $\sigma = \frac{1}{q}$ this quantity. We assume that the vortex is isolated and that the flow is inviscid, incompressible and without forcing. Under these conditions, σ is conserved :

$$\frac{D\sigma}{Dt} = 0 \tag{A22}$$

Now, we derive the linear Charney-Stern theorem for small disturbances to the parallel steady basic state, directly from the linearized equations of motion. We linearize the motion about the rotating flow which becomes a meridionnal basic state $\overline{v_y}(\varepsilon)$. In the basic state $\partial_\varepsilon = 0$, and thus $\partial_E = 0$. The velocity field takes the following form :

$$\vec{v}(\varepsilon, y, z, t) = v'_\varepsilon(\varepsilon, y, z, t)\vec{e_\varepsilon} + (\overline{v_y}(y, z) + v'_y(\varepsilon, y, z, t))\vec{e_y} + v'_z(\varepsilon, y, z, t)\vec{e_z} \tag{A23}$$

Now, the problem is similar to that of Kushner and Shepherd (1995). By neglecting the boundary terms, the pseudo-momentum equation is written :

$$\frac{\partial}{\partial t}\int_D \left(\frac{\sigma'^2}{2\overline{\sigma}\frac{\partial \overline{\sigma}}{\partial E}}\right) dD = 0 \tag{A24}$$

where D is the infinite space. Denoting $\langle\cdot\rangle$ the average on the $\vec{e_y}$ direction, the equation takes the following form :

$$\frac{\partial}{\partial t}\int\int \left(\frac{\langle\sigma'^2\rangle}{2\overline{\sigma}\frac{\partial \overline{\sigma}}{\partial E}}\right) d\varepsilon dz = 0 \tag{A25}$$

As a result, the quantity $\overline{\sigma}\frac{\partial \overline{\sigma}}{\partial E}$ must change sign and vanish for instability occurs. Taking into account that :

$$\overline{\sigma} = \frac{1}{q} \tag{A26}$$

$$\frac{\partial \overline{\sigma}}{\partial E} = \frac{\partial \overline{\sigma}}{\partial \varepsilon}\frac{\partial \varepsilon}{\partial E} \tag{A27}$$

$$\tag{A28}$$

We obtain :

$$\frac{\partial \overline{\sigma}}{\partial E} = -\frac{\overline{q}}{\overline{q}^4}\frac{\partial \overline{q}}{\partial \varepsilon}\frac{\partial \varepsilon}{\partial E} \tag{A29}$$

Therefore, the quantity $\overline{q}\frac{\partial \overline{q}}{\partial \varepsilon}\frac{\partial E}{\partial \varepsilon}$ must change sign for an instability to grow. This necessary condition for instability gathers three conditions :

- If $\overline{q}\frac{\partial \overline{q}}{\partial \varepsilon}$ keeps its sign then $\frac{\partial E}{\partial \varepsilon} = \omega_a/f_0$, where ω_a is the absolute vorticity, must change sign. We recover the necessary condition for anticyclonic ageostrophic instability (McWilliams et al., 2004) ;
- If $\frac{\partial \overline{q}}{\partial \varepsilon}\frac{\partial E}{\partial \varepsilon}$ keeps its sign then q must change sign and by repercution, the Ertel Potential Vorticity must change sign. We recover the necessary condition for symmetric instability with $f_0 > 0$ (Fjørtoft, 1950).
- Finally, if $\overline{q}$ keeps its sign then $\frac{\partial \overline{q}}{\partial \varepsilon}\frac{\partial E}{\partial \varepsilon}$ must change sign which the necessary condition for inertial instability (Eliassen, 1983). Indeed, $\frac{\partial \overline{q}}{\partial \varepsilon}$ represents the angular momentum and $\frac{\partial E}{\partial \varepsilon}$ its derivative with respect to ε.

The second condition gives us a restriction on α values. Regions where the Ertel Potential Vorticity becomes negative corresponds to regions where $\alpha > 1$. Therefore, from this theoretical necessary condition, we expect that $\alpha < 1$ for a large part of the eddy boundary. This statement is consistent with figure 10 which shows that α is smaller than 1 over 98% of the eddy boundary area.

References

Archer, M. R., Schaeffer, A., Keating, S. R., Roughan, M., Holmes, R. M., & Siegelman, L. (2020). Observations of submesoscale variability and frontal subduction within the mesoscale eddy field of the tasman sea. *Journal of Physical Oceanography*.

Benthuysen, J. A., & Thomas, L. N. (2012). Friction and diapycnal mixing at a slope: Boundary control of potential vorticity. *Journal of Physical Oceanography*, *42*, 1509-1523.

Beron-Vera, F. J., Wang, Y., Olascoaga, M. J., Goñi, G., & Haller, G. (2013). Objective detection of oceanic eddies and the agulhas leakage. *Journal of Physical Oceanography*, *43*, 1426-1438.

Bryden, H. L. (1979). Poleward heat flux and conversion of available potential energy in drake passage. *Journal of Marine Research*, *37*, 1-12.

Bulters, A. C. (2012). Three-dimensional structure of thermohaline staircases in the tropical north atlantic and their effect on acoustic propagation..

Carton, X., Flierl, G. R., & Polvani, L. M. (1989). The generation of tripoles from unstable axisymmetric isolated vortex structures. *Europhysics Letters*, *9*, 339–344.

Chaigneau, A., Eldin, G., & Dewitte, B. (2009). Eddy activity in the four major upwelling systems from satellite altimetry (1992-2007). *Progress in Oceanography*, *83*, 117-123.

Chelton, D., Schlax, M. G., & Samelson, R. M. (2011). Global observations of nonlinear mesoscale eddies. *Progress in Oceanography*, *91*, 167-216.

Chen, J., Tapley, B. D., Wilson, C. R., Cazenave, A., Seo, K., & Kim, J. (2020). Global ocean mass change from grace and grace follow-on and altimeter and argo measurements. *Geophysical Research Letters*, *47*.

de Marez, C., Meunier, T., Morvan, M., L'Hégaret, P., & Carton, X. (2020). Study of the stability of a large realistic cyclonic eddy. *Ocean Modelling*, *146*, 101540.

D'Addezio, J. M., Bingham, F. M., & Jacobs, G. A. (2019). Sea surface salinity subfootprint variability estimates from regional high-resolution model simulations. *Remote Sensing of Environment*.

Egger, J., & Chaudhry, Q. Z. (2009). Progress of research on potential vorticity and its inversion..

Eliassen, A. (1983). The charney-stern theorem on barotropic-baroclinic instability. *pure and applied geophysics*, *121*, 563-572.

Ertel, H. (1942). Ein neuer hydrodynamischer erhaltungssatz. *Naturwissenschaften*, *30*, 543-544.

Fer, I., Voet, G., Seim, K. S., Rudels, B., & Latarius, K. (2010). Intense mixing of the faroe bank channel overflow. *Geophysical Research Letters*, *37*, L02604.

Fjørtoft, R. (1950). Application of integral theorems in deriving criteria of stability for laminar flows and for the baroclinic circular vortex.

Flierl, G. R. (1981). Particle motions in large-amplitude wave fields. *Geophysical and Astrophysical Fluid Dynamics*, *18*, 39-74.

Frenger, I., Gruber, N., Knutti, R., & Münnich, M. (2013). Imprint of southern ocean eddies on winds, clouds and rainfall. *Nature Geoscience*, *6*, 608-612.

Halle, C., & Pinkel, R. (2003). Internal wave variability in the beaufort sea during the winter of 1993/1994. *Journal of Geophysical Research*, *108*, 3210.

Hoskins, B. J. (1982). The mathematical theory of frontogenesis. *Annual Review of Fluid Mechanics*, *14*, 131-151.

Hoskins, B. J., & Bretherton, F. P. (1972). Atmospheric frontogenesis models: Mathematical formulation and solution. *Journal of the Atmospheric Sciences*, *29*, 11–37.

Hunt, J. C. R., Leibovich, S., & Richards, K. J. (1988). Turbulent shear flows over low hills. *Quarterly Journal of the Royal Meteorological Society*, *114*, 1435-1470.

Ioannou, A., Speich, S., & Laxenaire, R. (2022). Characterizing mesoscale eddies of eastern upwelling origins in the atlantic ocean and their role in offshore transport. *Frontiers in Marine Science*.

Jayne, S. R., & Marotzke, J. (2002). The oceanic eddy heat transport. *Journal of Physical Oceanography*, *32*, 3328-3345.

Joyce, T. M. (1977). A note on the lateral mixing of water masses. *Journal of Physical Oceanography*, *7*, 626-629.

Joyce, T. M. (1984). Velocity and hydrographic structure of a gulf stream warm-core ring. *Journal of Physical Oceanography*, *14*, 936-947.

Katz, E. J. (1969). Further study of a front in the sargasso sea. *Tellus A*, *21*, 259-269.

Kushner, P. J., & Shepherd, T. G. (1995). Wave-activity conservation laws and stability theorems for semi-geostrophic dynamics. part 2. pseudoenergy-based theory. *Journal of Fluid Mechanics*, *290*, 105–129.

Laxenaire, R., Speich, S., Blanke, B., Chaigneau, A., Pegliasco, C., & Stegner, A. (2018). Anticyclonic eddies connecting the western boundaries of indian and atlantic oceans. *Journal of Geophysical Research: Oceans*.

Laxenaire, R., Speich, S., & Stegner, A. (2019). Evolution of the thermohaline structure of one agulhas ring reconstructed from satellite altimetry and argo floats. *Journal of Geophysical Research*, *124*, 8969-9003.

Laxenaire, R., Speich, S., & Stegner, A. (2020). Agulhas ring heat content and transport in the south atlantic estimated by combining satellite altimetry and argo profiling floats data. *Journal of Geophysical Research*, *125*.

Legras, B., & Dritschel, D. G. (1993). Vortex stripping and the generation of high vorticity gradients in two-dimensional flows. *Flow Turbulence and Combustion*, *51*, 445–455.

L'Hégaret, P., Carton, X., Louazel, S., & Boutin, G. (2015). Mesoscale eddies and submesoscale structures of persian gulf water off the omani coast in spring 2011. *Ocean Science*, *12*, 687-701.

L'Hégaret, P., Duarte, R., Carton, X., Vic, C., Ciani, D., Baraille, R., & Corréard, S. (2015). Mesoscale variability in the arabian sea from hycom model results and observations: impact on the persian gulf water path. *Ocean Science*, *11*, 667-693.

L'Hégaret, P., Schütte, F., Speich, S., Reverdin, G., Baranowski, D. B., Czeschel, R., … others (2022). Ocean cross-validated observations from the r/vs l'atalante, maria s. merian and meteor and related platforms as part of the eurec 4 a-oa/atomic campaign. *Earth System Science Data Discussions*, 1–39.

Lozier, M. S. (1997). Evidence for large-scale eddy-driven gyres in the north atlantic. *Science*, *277*, 361-364.

Lumpkin, R. (2016). Global characteristics of coherent vortices from surface drifter trajectories. *Journal of Geophysical Research*, *121*, 1306-1321.

Mariotti, A., Legras, B., & Dritschel, D. G. (1994). Vortex stripping and the erosion of coherent structures in two-dimensional flows. *Physics of Fluids*, *6*, 3954–3962.

Marshall, J., & Schott, F. A. (1999). Open-ocean convection: Observations, theory, and models. *Reviews of Geophysics*, *37*, 1 - 64.

Marshall, J., & Speer, K. (2012). Closure of the meridional overturning circulation through southern ocean upwelling. *Nature Geoscience*, *5*, 171-180.

Martin, A. P., Richards, K. J., Bracco, A., & Provenzale, A. (2002). Patchy productivity in the open ocean. *Global Biogeochemical Cycles*, *16*.

McWilliams, J. C., Molemaker, M., & Yavneh, I. (2004). Ageostrophic, anticyclonic instability of a geostrophic, barotropic boundary current. *Physics of Fluids*, *16*, 3720-3725.

Morel, Y., Gula, J., & Ponte, A. L. (2019). Potential vorticity diagnostics based on balances between volume integral and boundary conditions. *Ocean Modelling*.

Morrow, R., Coleman, R., Church, J. A., & Chelton, D. (1994). Surface eddy momentum flux and velocity variances in the southern ocean from geosat altimetry. *Journal of Physical Oceanography*, *24*, 2050-2071.

Morrow, R., & Traon, P.-Y. L. (2012). Recent advances in observing mesoscale ocean dynamics with satellite altimetry. *Advances in Space Research*, *50*, 1062-1076.

Morvan, M., L'Hégaret, P., Carton, X., Gula, J., Vic, C., de Marez, C., … Koshel, K. V. (2019). The life cycle of submesoscale eddies generated by topographic interactions. *Ocean Science*, *15*, 1531-1543.

Nencioli, F., Kuwahara, V. S., Dickey, T. D., Rii, Y. M., & Bidigare, R. R. (2008). Physical dynamics and biological implications of a mesoscale eddy in the lee of hawai'i : Cyclone opal observations during e-flux iii. *Deep-sea Research Part II-Topical Studies in Oceanography*, *55*, 1252–1274.

Nencioli, F., Nencioli, F., Petrenko, A. A., & Doglioli, A. M. (2016). Diagnosing cross-shelf transport along an ocean front: An observational case study in the gulf of lion. *Journal of Geophysical Research*, *121*, 7218-7243.

Paillet, J., Cann, B. L., Carton, X., Morel, Y., & Serpette, A. (2002). Dynamics and evolution of a northern meddy. *Journal of Physical Oceanography*, *32*, 55–79.

Peliz, A., Boutov, D., Aguiar, A. C. B., & Carton, X. (2014). The gulf of cadiz gap wind anticyclones. *Continental Shelf Research*, *91*, 171-191.

Pinot, J. M., Tintoré, J., Lopezjurado, J., Depuelles, M., & Jansa, J. (1995). Three-dimensional circulation of a mesoscale eddy/front system and its biological implications. *Oceanologica Acta*, *18*, 389-400.

Rhines, P. B. (1975). Waves and turbulence on a beta-plane. *Journal of Fluid Mechanics*, *69*, 417–443.

Richardson, P. L., & Tychensky, A. (1998). Meddy trajectories in the canary basin measured during the semaphore experiment, 1993–1995. *Journal of Geophysical Research*, *103*, 25029-25045.

Ruddick, B. R., & Gargett, A. E. (2003). Oceanic double-diffusion: introduction [progress in oceanography 56 (2003) 381–393]. *Progress in Oceanography*, *57*, 237-237.

Ruddick, B. R., Oakey, N. S., & Hebert, D. (2010). Measuring lateral heat flux across a thermohaline front: A model and observational test. *Journal of Marine Research*, *68*, 523-539.

Rudnick, D. L. (2001). On the skewness of vorticity in the upper ocean. *Geophysical Research Letters*, *28*.

Sallée, J., Speer, K., Rintoul, S. R., & Wijffels, S. E. (2010). Southern ocean thermocline ventilation. *Journal of Physical Oceanography*, *40*, 509-529.

Shcherbina, A. Y., D'Asaro, E. A., Lee, C. M., Klymak, J. M., Molemaker, M., & McWilliams, J. C. (2013). Statistics of vertical vorticity, divergence, and strain in a developed submesoscale turbulence field. *Geophysical Research Letters*, *40*, 4706–4711.

Smith, W. H. F., & Sandwell, D. T. (1997). Global sea floor topography from satellite altimetry and ship depth soundings. *Science*, *277*, 1956-1962.

Speich, S., & Team, E. S. (2021). *Eurec4a-oa cruise report, 19 january - 19 february 2020, vessel : L'atalante.* Retrieved from `http://doi.org/10.13155/80129` doi: 10.13155/80129

Voorhis, A. D., & Hersey, J. (1964). Oceanic thermal fronts in the sargasso sea. *Journal of Geophysical Research*, *69*, 3809-3814.

Weiss, J. (1991). The dynamics of entropy transfer in two-dimensional hydrodynamics. *Physica D: Nonlinear Phenomena*, *48*, 273-294.

Welander, P. (1973). Lateral friction in the oceans as an effect of potential vorticity mixing. *Geophysical and Astrophysical Fluid Dynamics*, *5*, 173-189.

Wunsch, C. (1999). Where do ocean eddy heat fluxes matter. *Journal of Geophysical Research*, *104*, 13235-13249.

Zhang, Y., Wu, G., Liu, Y., & Guan, Y. (2014). The effects of asymmetric potential vorticity forcing on the instability of south asia high and indian summer monsoon onset. *Science China Earth Sciences*, *57*, 337–350.

Ōkubo, A. (1970). Horizontal dispersion of floatable particles in the vicinity of velocity singularities such as convergences. *Deep Sea Research and Oceanographic Abstracts*, *17*, 445-454.

Figure 1.

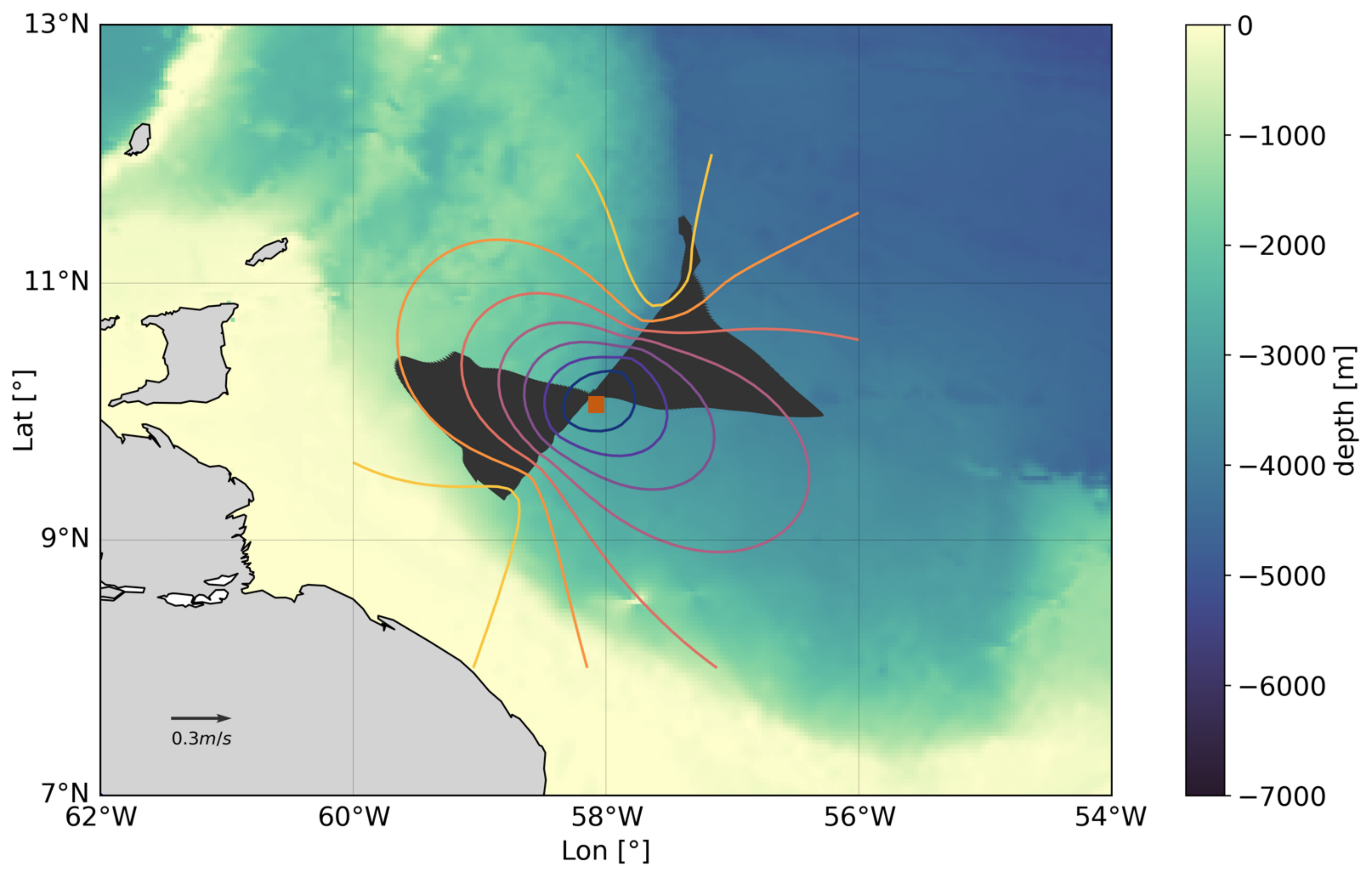

13°N
11°N
9°N
7°N
62°W
60°W
58°W
56°W
54°W
Lat [°]
Lon [°]
0.3m/s
0
−1000
−2000
−3000
−4000
−5000
−6000
−7000
depth [m]

Figure 2.

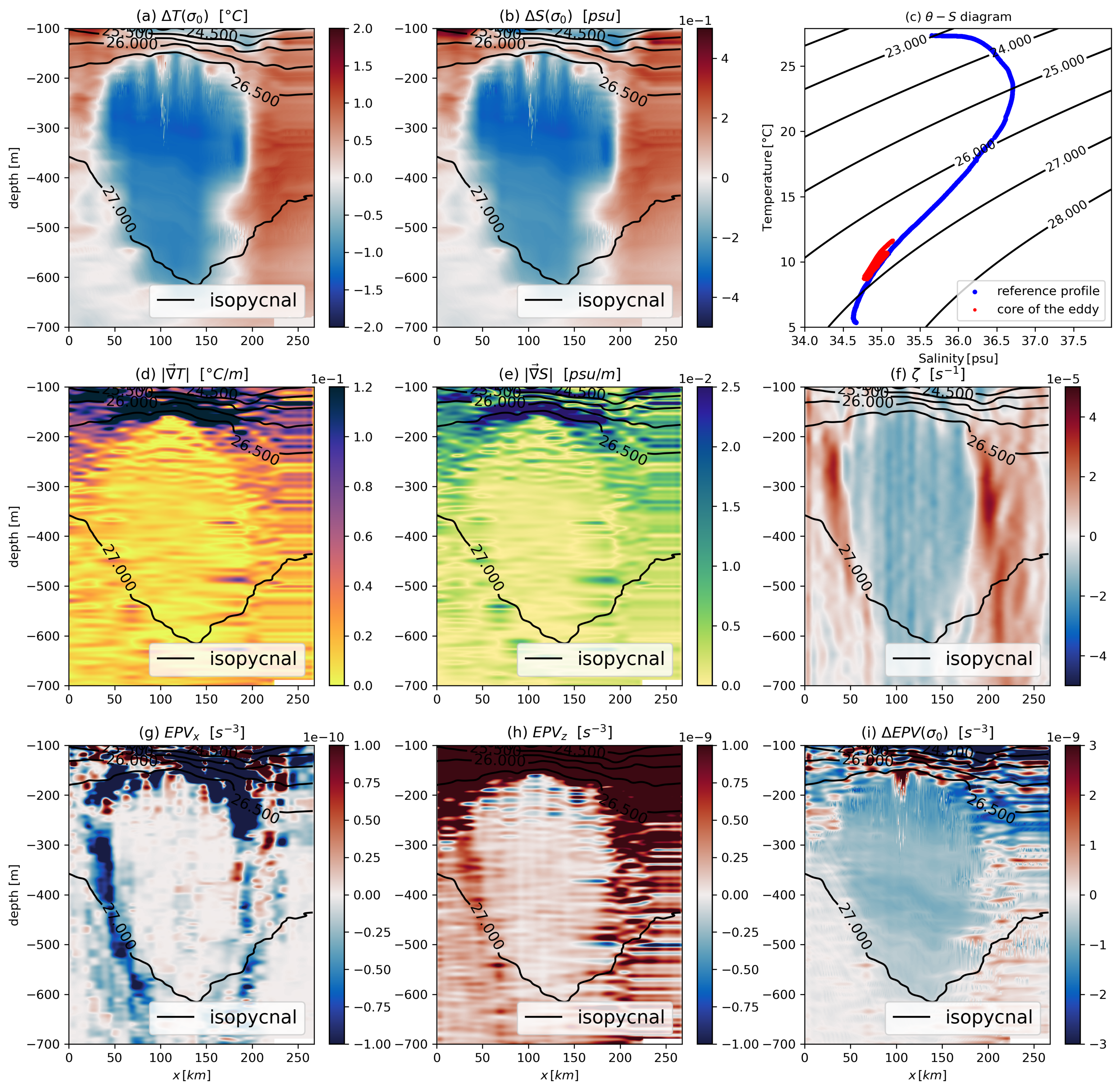

(a) $\Delta T(\sigma_0)$ [°C]
(b) $\Delta S(\sigma_0)$ [psu]
(c) $\theta - S$ diagram
Temperature [°C]
Salinity [psu]
reference profile
core of the eddy
(d) $|\vec{\nabla} T|$ [°C/m]
(e) $|\vec{\nabla} S|$ [psu/m]
(f) ζ [s^{-1}]
(g) EPV_x [s^{-3}]
(h) EPV_z [s^{-3}]
(i) $\Delta EPV(\sigma_0)$ [s^{-3}]
depth [m]
x [km]
isopycnal

Figure 3.

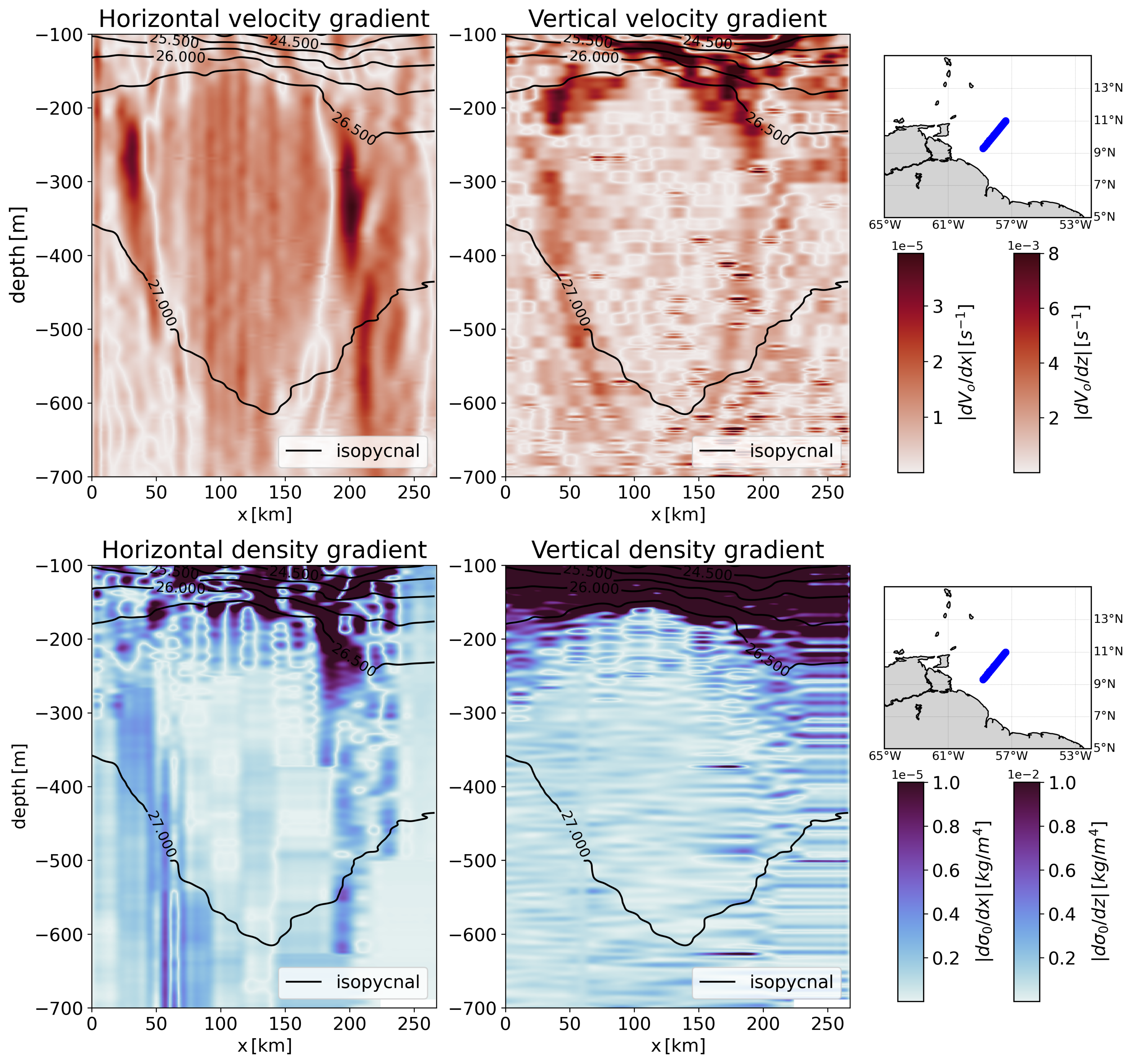

Horizontal velocity gradient
Vertical velocity gradient
Horizontal density gradient
Vertical density gradient
depth [m]
x [km]
isopycnal
25.500
24.500
26.000
26.500
27.000
1e-5
1e-3
1e-2
$|dV_o/dx|\,[s^{-1}]$
$|dV_o/dz|\,[s^{-1}]$
$|d\sigma_0/dx|\,[kg/m^4]$
$|d\sigma_0/dz|\,[kg/m^4]$
65°W
61°W
57°W
53°W
13°N
11°N
9°N
7°N
5°N

Figure 4.

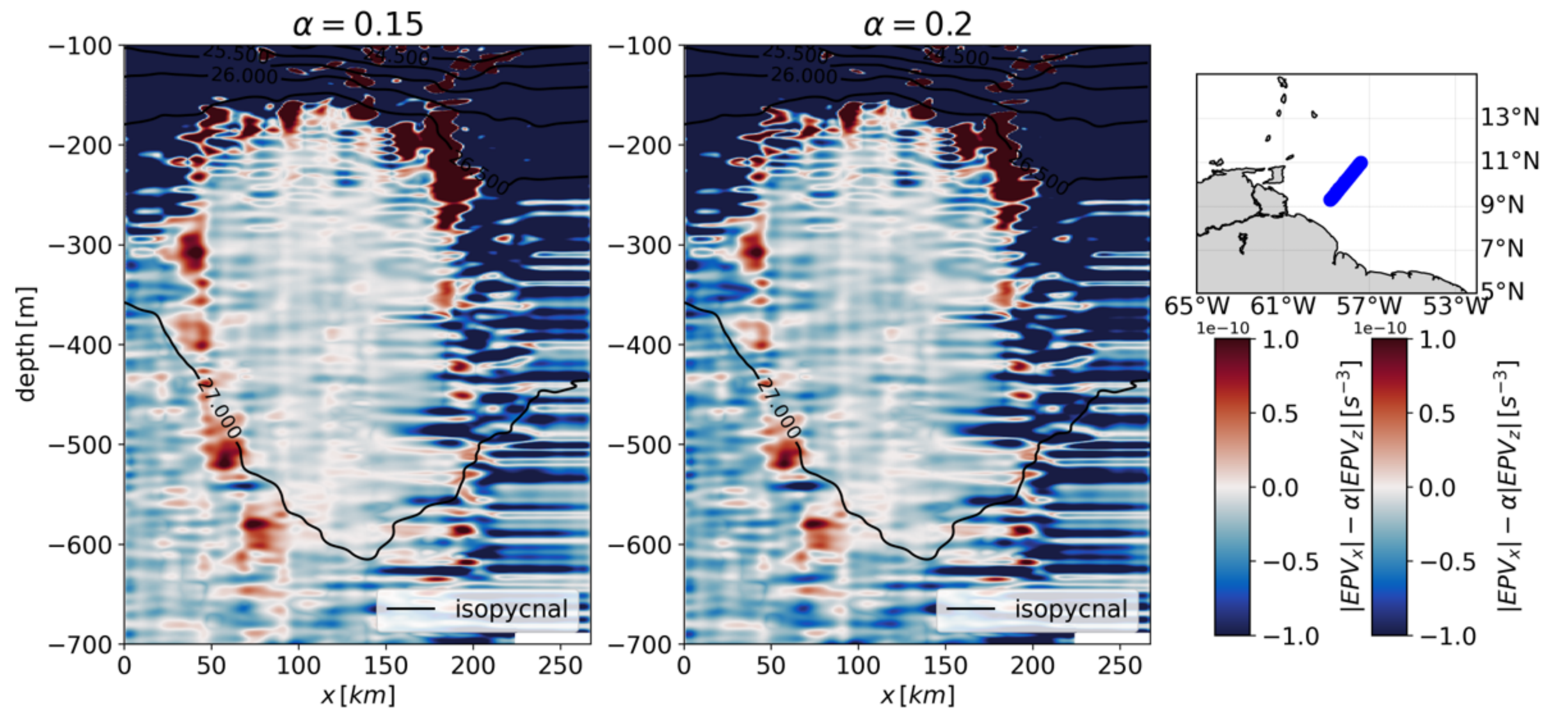

$\alpha = 0.15$
$\alpha = 0.2$
depth [m]
x [km]
isopycnal
25.500
24.500
26.000
26.500
27.000
13°N
11°N
9°N
7°N
5°N
65°W
61°W
57°W
53°W
1e−10
$|EPV_x| - \alpha|EPV_z|\,[s^{-3}]$

Figure 5.

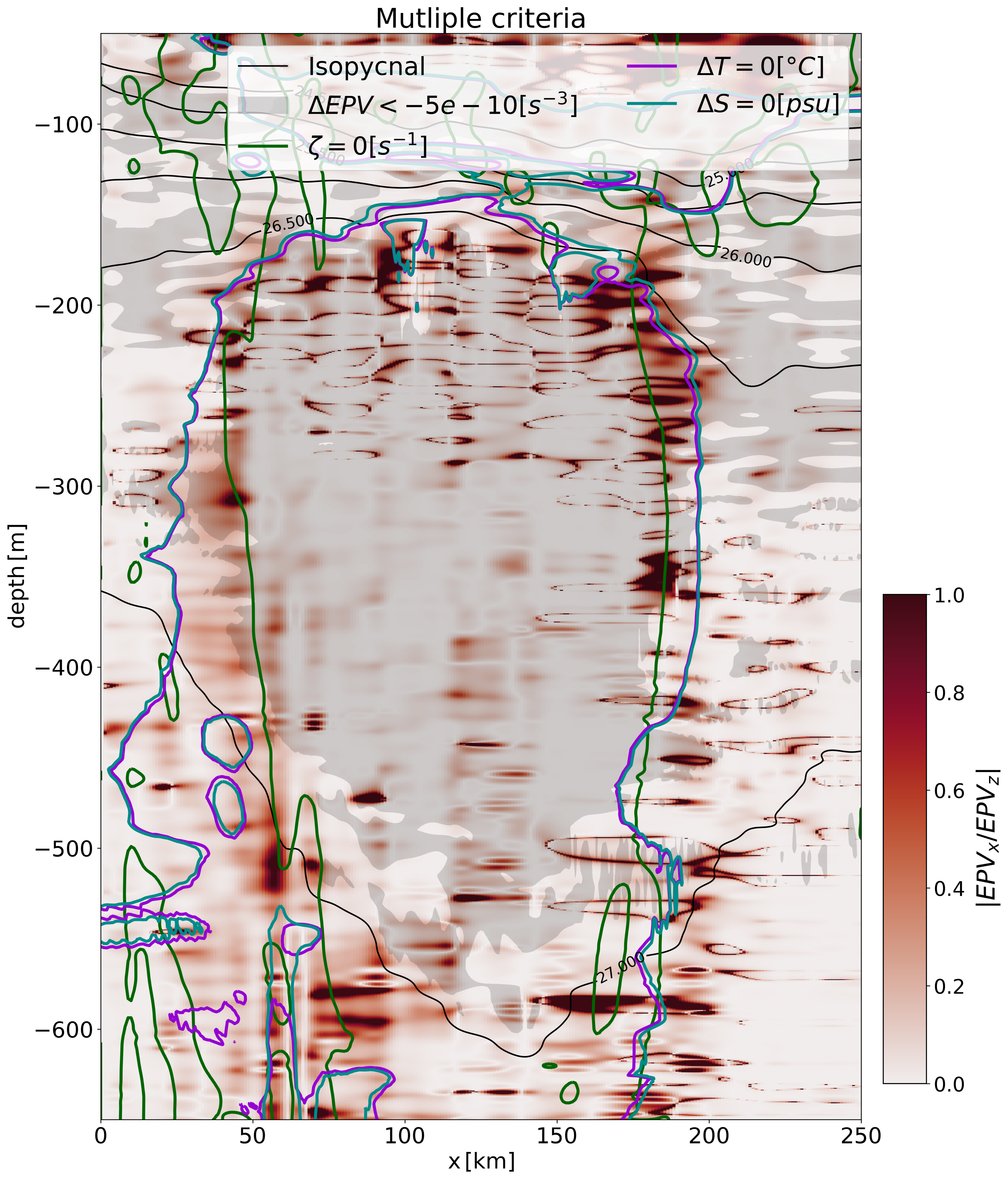

Mutliple criteria
Isopycnal
$\Delta EPV < -5e-10[s^{-3}]$
$\zeta = 0[s^{-1}]$
$\Delta T = 0[°C]$
$\Delta S = 0[psu]$
26.500
26.000
25.000
27.000
−100
−200
−300
−400
−500
−600
depth [m]
0
50
100
150
200
250
x [km]
1.0
0.8
0.6
0.4
0.2
0.0
$|EPV_x/EPV_z|$

Figure 6.

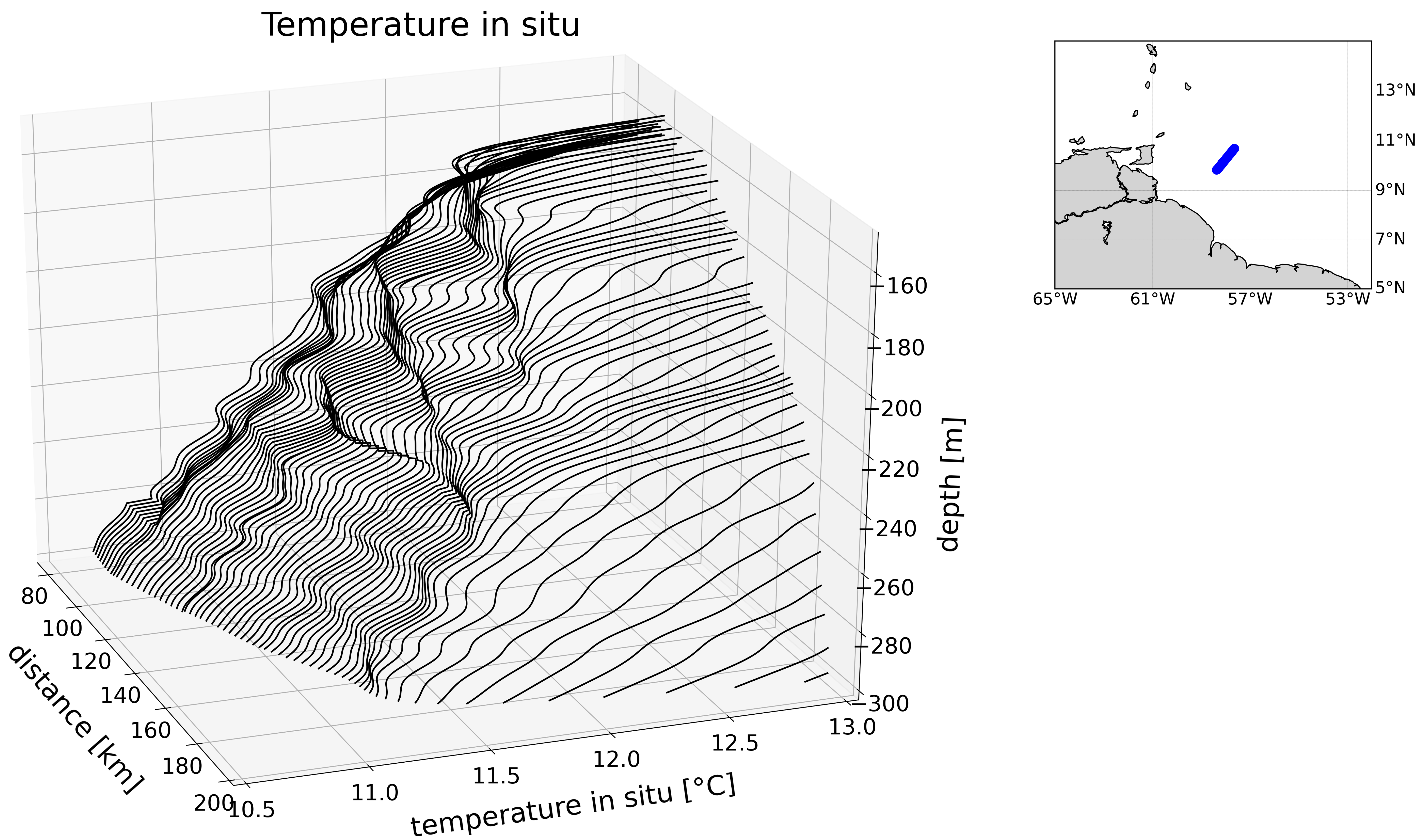
Temperature in situ
distance [km]
80
100
120
140
160
180
200
temperature in situ [°C]
10.5
11.0
11.5
12.0
12.5
13.0
depth [m]
160
180
200
220
240
260
280
300
13°N
11°N
9°N
7°N
5°N
65°W
61°W
57°W
53°W

Figure 7.

$$\boxed{\text{Data}} \xrightarrow[(1)]{} \underset{(2)}{\boxed{\Delta T(\sigma_0), \Delta S(\sigma_0)}} \xrightarrow[(3)]{} \boxed{\Delta b} \xrightarrow[(4)]{} \boxed{V_o} \xrightarrow[(5)]{} \boxed{EPV_x, EPV_z} \longrightarrow \boxed{\frac{|EPV_x|}{|EPV_z|}}$$

Figure 8.

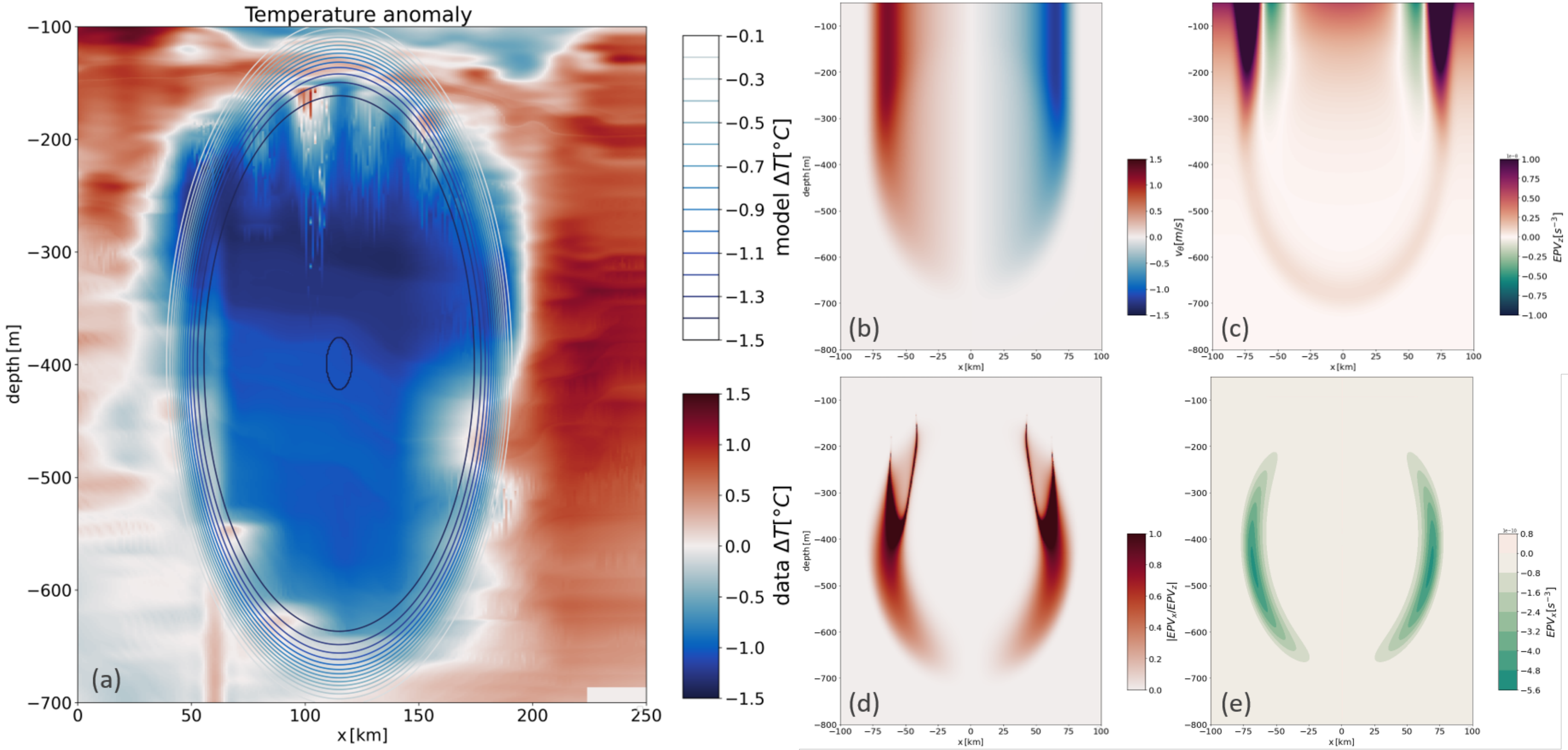

Temperature anomaly
depth [m]
x [km]
model ΔT[°C]
data ΔT[°C]
(a)
(b)
(c)
(d)
(e)
$v_\theta [m/s]$
$EPV_z [s^{-3}]$
$|EPV_x/EPV_z|$
$EPV_x [s^{-3}]$

Figure 9.

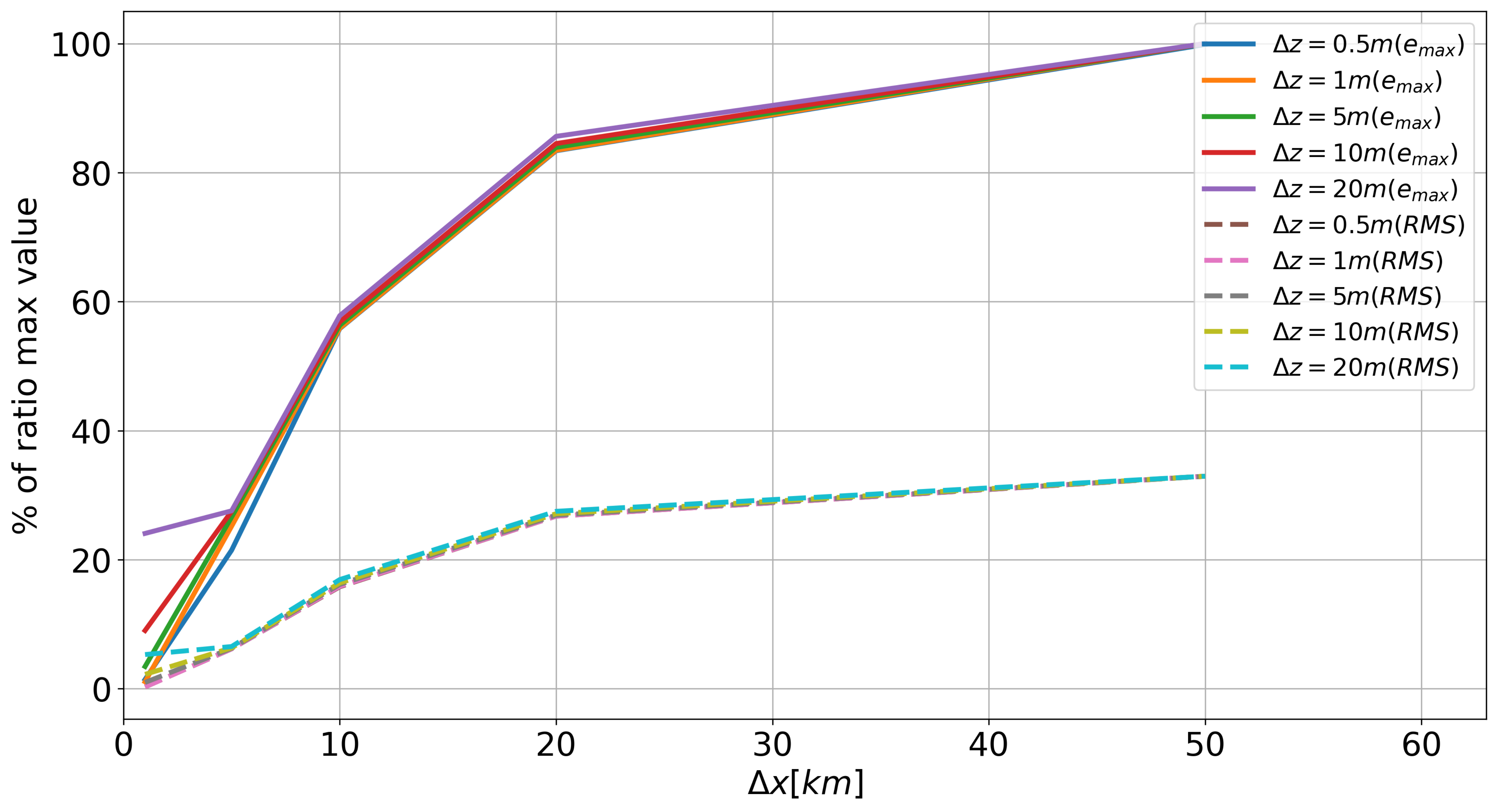

100
80
60
40
20
0
0
10
20
30
40
50
60
% of ratio max value
$\Delta x[km]$
$\Delta z = 0.5m(e_{max})$
$\Delta z = 1m(e_{max})$
$\Delta z = 5m(e_{max})$
$\Delta z = 10m(e_{max})$
$\Delta z = 20m(e_{max})$
$\Delta z = 0.5m(RMS)$
$\Delta z = 1m(RMS)$
$\Delta z = 5m(RMS)$
$\Delta z = 10m(RMS)$
$\Delta z = 20m(RMS)$

Figure 10.

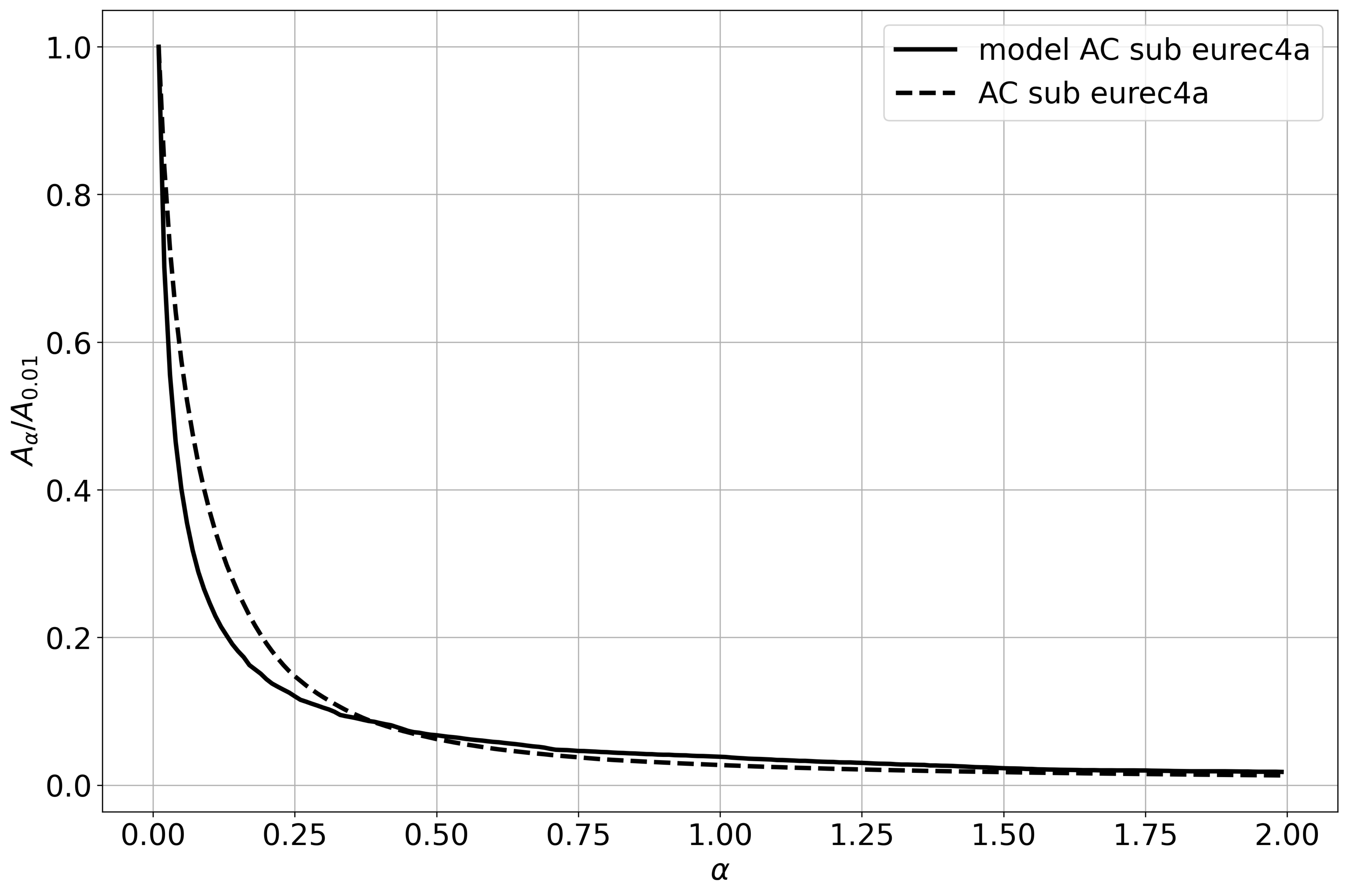

model AC sub eurec4a
AC sub eurec4a
$A_\alpha/A_{0.01}$
α
1.0
0.8
0.6
0.4
0.2
0.0
0.00
0.25
0.50
0.75
1.00
1.25
1.50
1.75
2.00

Figure 11.

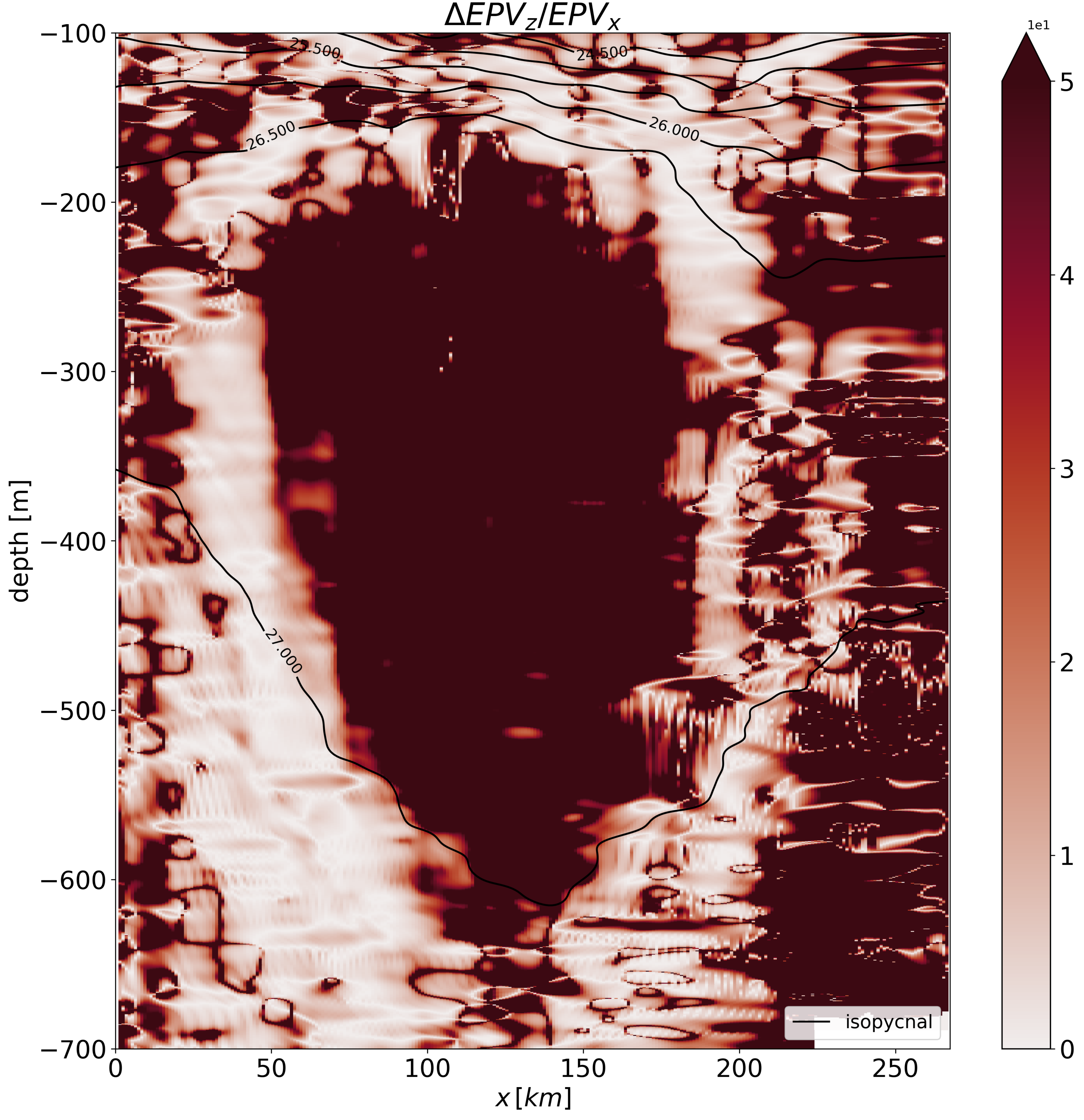

$\Delta EPV_z/EPV_x$
depth [m]
$x\,[km]$
-100
-200
-300
-400
-500
-600
-700
0
50
100
150
200
250
25.500
24.500
26.500
26.000
27.000
isopycnal
1e1
5
4
3
2
1
0

Figure 12.

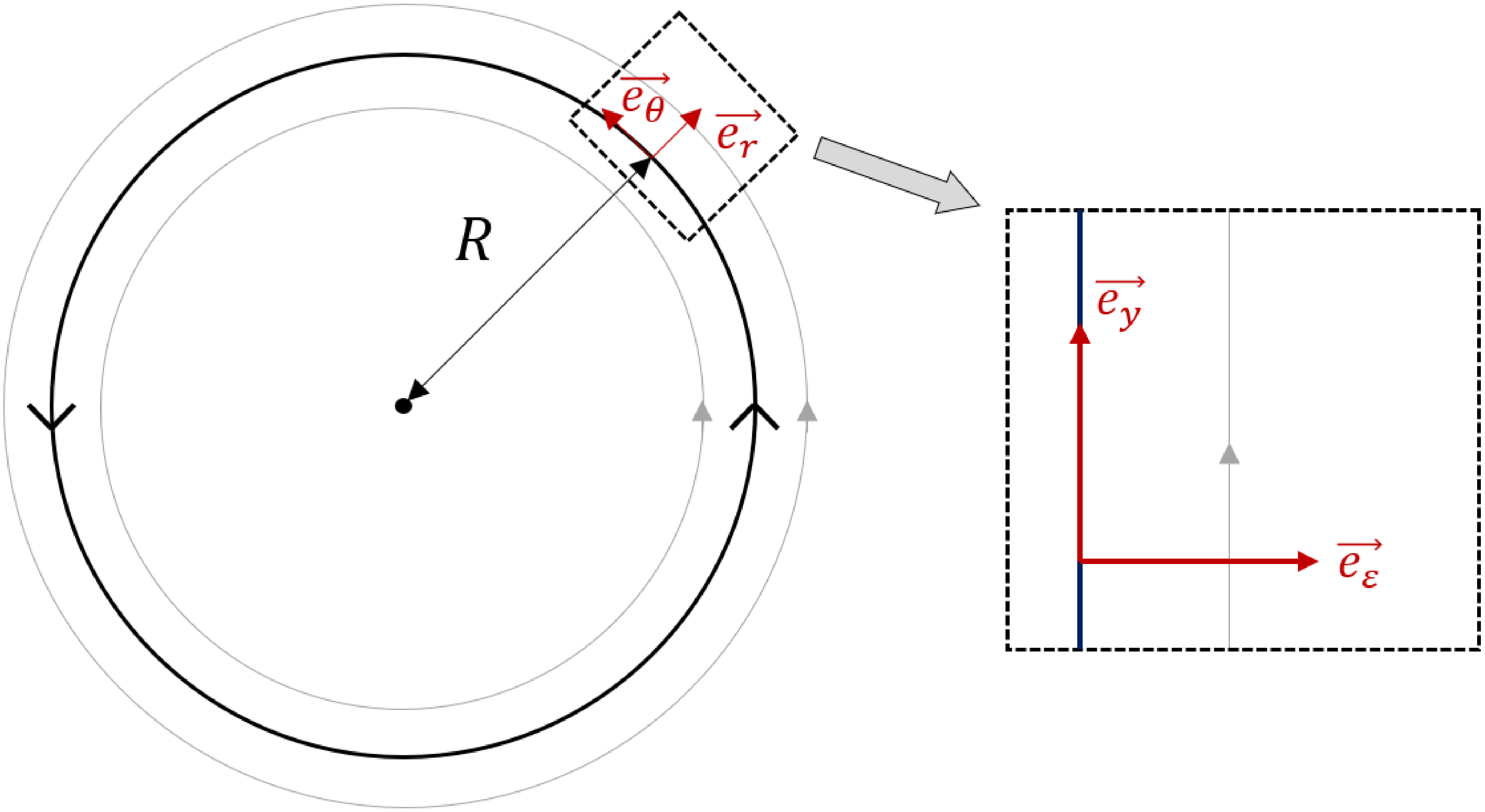

$\overrightarrow{e_\theta}$
$\overrightarrow{e_r}$
R
$\overrightarrow{e_y}$
$\overrightarrow{e_\varepsilon}$